



A11103 896230

REFERENCE

NIST
PUBLICATIONS

NISTIR 4931

Research for Electric Energy Systems — An Annual Report

William E. Anderson
Editor

U.S. DEPARTMENT OF COMMERCE
Technology Administration
National Institute of Standards
and Technology
Electronics and Electrical Engineering
Laboratory
Electricity Division
Gaithersburg, MD 20899

Prepared for
Department of Energy
Division of Electric Energy Systems
1000 Independence Avenue, SW
Washington, DC 20585

QC
100
U56
4931
1992

NIST

100
.456
4931
1992
R

NISTIR 4931

Research for Electric Energy Systems — An Annual Report

William E. Anderson
Editor

U.S. DEPARTMENT OF COMMERCE
Technology Administration
National Institute of Standards
and Technology
Electronics and Electrical Engineering
Laboratory
Electricity Division
Gaithersburg, MD 20899

Prepared for
Department of Energy
Division of Electric Energy Systems
1000 Independence Avenue, SW
Washington, DC 20585

December 1991

Issued June 1992



U.S. DEPARTMENT OF COMMERCE
Barbara Hackman Franklin, Secretary

TECHNOLOGY ADMINISTRATION
Robert M. White, Under Secretary for Technology

**NATIONAL INSTITUTE OF STANDARDS
AND TECHNOLOGY**
John W. Lyons, Director

Foreword

This report summarizes the progress of four technical investigations conducted during CY 91. Although reasonable efforts have been made to ensure the reliability of the data presented, it must be emphasized that this is an interim progress report and that further experimentation and analysis may be performed before the conclusions from any of these investigations are formally published. It is therefore possible that some of the observations presented in this report will be modified, expanded, or clarified by our subsequent research¹.

¹The identification of commercial materials and their sources is made to describe the experiment adequately. In no case does this identification imply recommendation by the National Institute of Standards and Technology, nor does it imply that the product is the best available.

Table of Contents

1	ELECTRIC FIELD MEASUREMENTS	1
1.1	Introduction	1
1.2	In Vitro Exposure Parameters With ELF Magnetic Fields	2
1.3	Measurements of Ion Mobility at Hydro-Quebec	6
2	GASEOUS DIELECTRICS RESEARCH	10
2.1	Introduction	10
2.2	Rate of S ₂ F ₁₀ Production from Negative Corona in Compressed SF ₆ .	11
2.2.1	Introduction	11
2.2.2	Measurement Method	12
2.2.3	Results	15
2.2.4	Discussion and Conclusions	18
2.3	Electron Scattering and Dissociative Attachment	19
2.3.1	Introduction	19
2.3.2	Experiment	20
2.3.3	Experimental Results and Discussion	20
2.3.4	Dissociative Attachment Rates in SF ₆	29
2.3.5	Conclusions	31
3	PARTIAL DISCHARGE AND DIELECTRIC LIQUID RESEARCH	32
3.1	Liquid Dielectrics	32
3.1.1	Introduction	32
3.1.2	Breakdown Test Method	32
3.1.3	Perfluorinated Polyether	34
3.1.4	Results	35
3.1.5	Positive Streamer Initiation in PFPE	41
3.1.6	Ditolyl Ether	42
3.1.7	Benzyl and Dibenzyl Toluene	42
3.1.8	Discussion and Conclusions	42
3.2	Partial Discharge Measurements	46
3.2.1	Introduction	46
3.2.2	Significance of Memory Propagation	46
3.2.3	Real-Time Stochastic Analyzer	47
3.2.4	Experimental Arrangement	51
3.2.5	Examples of Results	52

3.2.6	Discussion	57
4	FAST TRANSIENT MEASUREMENTS	60
4.1	Introduction	60
4.2	Kerr Cell Measurements	60
4.3	Kerr Cell Constant Determination	62
4.4	Results and Discussion	68
4.5	Conclusions	72
5	REFERENCES	74

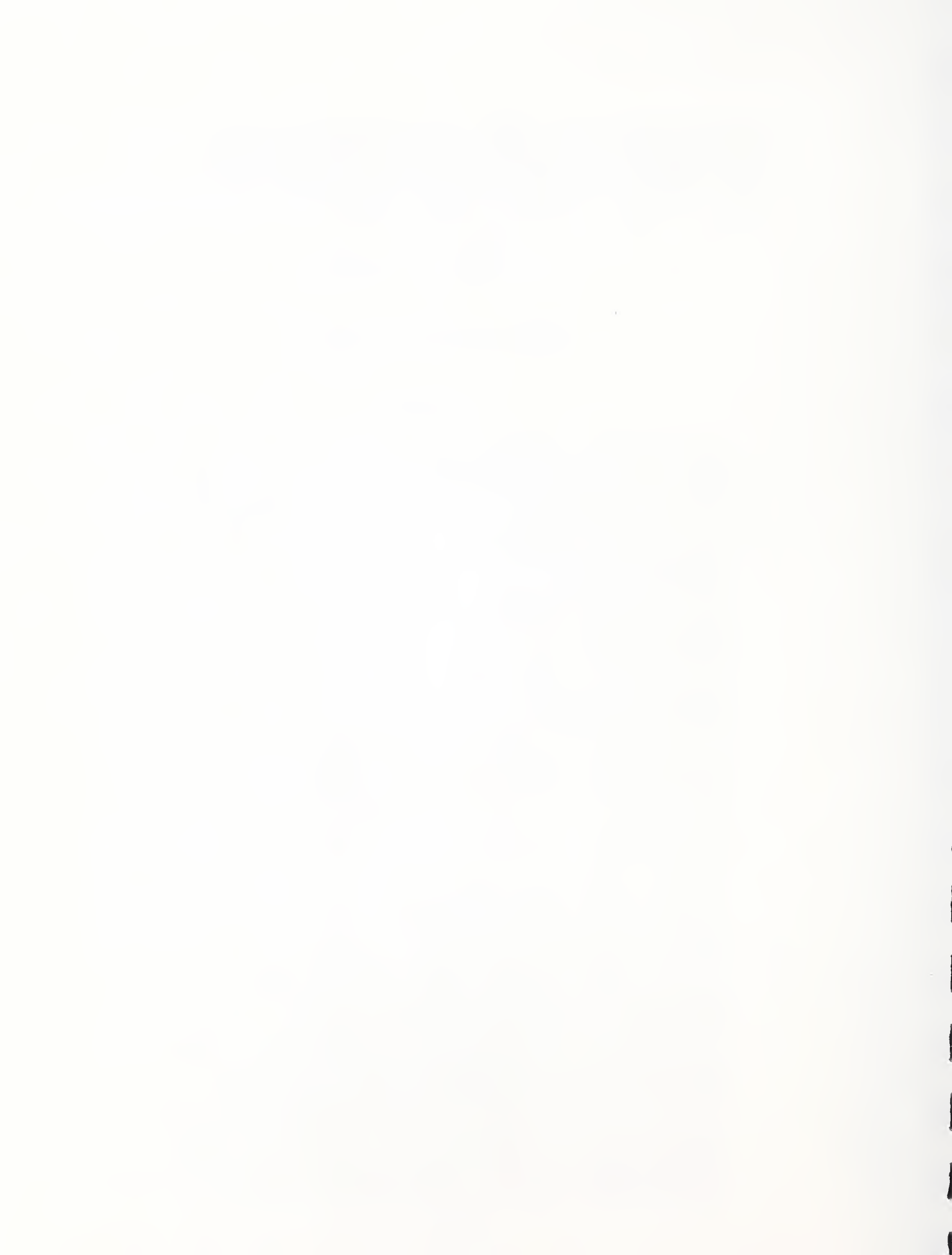
Research for Electric Energy Systems – An Annual Report

William E. Anderson, Editor

Abstract

This report documents the technical progress in the four investigations which make up the project "Support of Research Projects for Electrical Energy Systems", Department of Energy Task Order Number 137, funded by the U.S. Department of Energy and performed by the Electricity Division of the National Institute of Standards and Technology (NIST). The first investigation is concerned with the measurement of magnetic fields in support of epidemiological and in vitro studies of biological field effects. Theoretical comparisons were made of induced current densities, electric fields, and rates of energy deposition in a cylindrical volume of culture medium for linearly and circularly polarized magnetic fields. Measurements of air ion mobility spectra were performed in a dc electric field/air ion exposure system for humans. Consultations with various state and federal organizations and the development of standards related to electric and magnetic field measurements continued. The second investigation is concerned with two different activities: the production of S_2F_{10} in negative corona in SF_6 and the measurement of electron scattering and dissociative electron attachment cross sections for SF_6 and its electrical-discharge by-products. The production rates of S_2F_{10} in SF_6 are found to be quite reproducible and suggest a reliable method for preparing reference gas samples containing known trace levels of S_2F_{10} in SF_6 . The SF_6 cross section measurements are useful to calculate dissociative-attachment rate coefficients for SF_6 by-products in SF_6 . The third investigation is also concerned with two different activities: several liquids that are currently used or have potential for use as high voltage dielectrics are studied using conventional impulse breakdown measurement techniques and high-speed photography and advances in partial discharge measurement techniques are presented. The measurements on liquid dielectrics demonstrate that the techniques described can provide useful information on the relative strengths of the candidate materials if proper care is taken. The partial discharge measurement system developed at NIST, the SAPP (Stochastic Analyzer for Pulsating Phenomena) has been extended to ac conditions. The results are described. The last investigation is concerned with the evaluation and improvement of methods for measuring fast transients in electrical power systems such as might be associated with an electromagnetic impulse. Kerr cells have been used for several years by NIST and others

for measuring high voltages. Recent work is presented which enables a more accurate determination of the Kerr cell constant using state-of-the-art curve-fitting techniques. The results show the advantage of this new method.



1 ELECTRIC FIELD MEASUREMENTS

Task 01

Martin Misakian

Electricity Division

National Institute of Standards and Technology

1.1 Introduction

The objectives of this project are to develop methods to evaluate and calibrate instruments which are used, or are being developed, to characterize electrical parameters in the vicinity of power lines and in laboratory exposure systems designed to simulate the power-line environment. Electrical measurement support is also provided for Department of Energy-supported research to determine whether there are biological effects due to ac fields and dc fields with ions.

During 1991, theoretical comparisons were made of induced current densities, electric fields, and rates of energy deposition in a cylindrical volume of culture medium during in vitro studies with linearly and circularly polarized extremely low frequency (ELF) magnetic fields. The results of this study were published in the journal *Bioelectromagnetics* [1], and most of the text is reproduced below.

At the request of researchers at Hydro-Quebec, measurements of air ion mobility spectra were performed in a dc electric field/air ion exposure system for humans. Consultations were also held on measuring dc electric fields, ion current density and monopolar charge density. These activities were supported by Hydro-Quebec and some measurement results are presented below.

Other events and activities related to the NIST Fields Project during 1991 included (a) measurements and model calculations of power-line magnetic fields near the NIST/Boulder day care facilities (completion of study begun in 1990), (b) preparation of portions of a primer on conducting in vitro studies with ELF magnetic and electric fields (scheduled for completion in 1992), (c) participation on research planning committees for the Health Effects Institute and the Bioelectromagnetics Society, (d) technical consultations with the FDA on a draft standard for measuring electric and magnetic fields near visual display terminals, (e) technical consultations with the National Toxicology Program and NIH during evaluations of research proposals, (f) participation on advisory panels for the California Department of Health Services and the National Cancer Institute, (g) leading an IEEE Power Engineering Society task force during preparation of a working group paper describing a protocol for measuring magnetic fields in residences (scheduled for completion in 1992), (h) invited speaker at a National Cancer Institute workshop on ELF field effects, (i) invited participant of an EPRI sponsored workshop on ELF field exposure assessment and, (j) a site visit

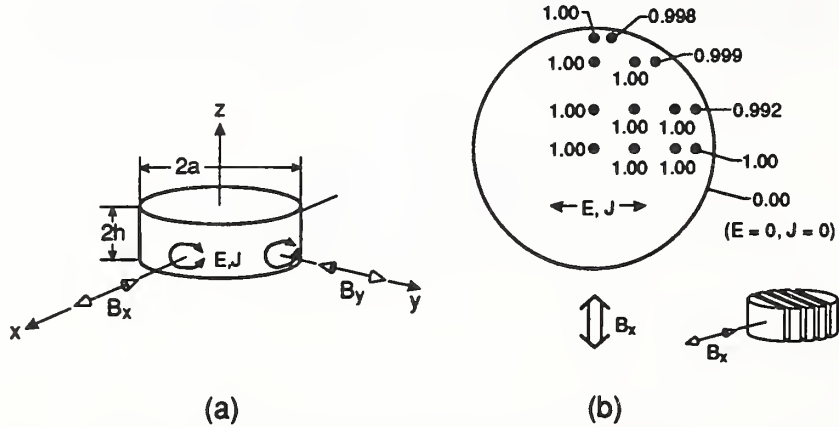


Figure 1. (a) Experimental configuration for in vitro studies with components of magnetic field applied parallel to x - and y -axes (b) normalized induced current density distribution along bottom (or top) surface of culture medium for uniform magnetic field parallel to x -axis for $2a = 6$ cm and $2h = 0.2$ cm.

to the University of Kentucky on behalf of EPRI, during which magnetic fields in a biological exposure system were characterized. The author also received the IEEE Standards Medallion award for his contributions in the preparation of standards for characterizing electrical parameters near ac and dc power lines.

1.2 In Vitro Exposure Parameters With ELF Magnetic Fields

Because multiphase power lines will, in general, produce rotating magnetic fields, some in vitro bioeffects experiments have been conducted with circularly polarized magnetic fields. Very often, however, the magnetic fields used are linearly polarized. This report examines the differences in candidate exposure parameters that are induced in culture medium by either linearly or circularly polarized magnetic fields. An experimental geometry is chosen that is commonly used during in vitro studies and that simplifies some of the calculations of the induced quantities. The information developed below complements that found in an earlier paper on exposure parameters during in vitro studies with ac magnetic fields [2].

Fig. 1a shows a cylindrical volume of culture medium of diameter $2a$ and depth $2h$ with extremely low frequency (ELF) magnetic fields applied along the x - and y -axes. Using equations developed by McLeod *et al.* [3] for rectangular geometries and vertically slicing the cylinder into approximately rectangular sections, it is readily shown that for $2a \gg 2h$, the induced current density and electric field at most locations on the top and bottom surfaces of the culture medium are uniform. Fig. 1b shows normalized values of induced current density on the bottom surface of a liquid

volume 6 cm in diameter and 0.2 cm deep, due to a magnetic field aligned with the x-axis.

Using the principle of superposition, the induced current density at the bottom surface of a rectangular section due to magnetic field components along the x- and y-axes is given by

$$\vec{J} = J_x \hat{i} + J_y \hat{j} \quad (1)$$

where [3]

$$J_x \simeq \frac{\omega \sigma B_y 2w}{\pi^2} \sum_{n_{\text{odd}}} \frac{4}{n^2} \left(\pm \cos\left(\frac{n\pi x}{2w}\right) \right) \left(\tanh\left(\frac{-n\pi h}{2w}\right) \right)$$

and

$$J_y \simeq \frac{\omega \sigma B_x 2w}{\pi^2} \sum_{m_{\text{odd}}} \frac{4}{m^2} \left(\pm \cos\left(\frac{m\pi y}{2w}\right) \right) \left(\tanh\left(\frac{-m\pi h}{2w}\right) \right).$$

In Eq. (1), ω is 2π times the frequency f ; σ is the conductivity of the culture medium; B_x and B_y are the ELF magnetic flux densities parallel to the x- and y-axes respectively; $2w$ is the width of a rectangular section ($2w \gg 2h$); \hat{i} and \hat{j} are unit vectors along the x- and y-axes; and, the \pm sign indicates that the sign in the summations alternates. For most values of x and y on the bottom and top surfaces of the culture medium, the product of w and the summations in the expressions for J_x and J_y are constant and equal to one another. Therefore, the vector components of current density can be expressed as

$$J_x = C B_y, \quad (2)$$

and

$$J_y = C B_x, \quad (3)$$

where C is a constant given by

$$C = \frac{\omega \sigma 2w}{\pi^2} \times (\text{summation}).$$

For a linearly polarized magnetic field where $B_x = B_o \sin \omega t$ and $B_y = B_o \sin \omega t$, the induced current density is also linearly polarized as shown at representative points (on bottom surface) in Fig. 2a. Similarly, for a circularly polarized magnetic field where $B_x = B_o \sin \omega t$ and $B_y = B_o \cos \omega t$, the induced current density is circularly polarized as shown at some instant for several representative points in Fig. 2b.

From Eqs. (1-3), the magnitude of the current density induced by a linearly polarized magnetic field, J_l , is

$$J_l = \sqrt{J_x^2 + J_y^2} = C B_o \sqrt{2} \sin \omega t. \quad (4)$$

Similarly, the magnitude of the current density induced by a circularly polarized magnetic field, J_o , is

$$J_o = C B_o. \quad (5)$$

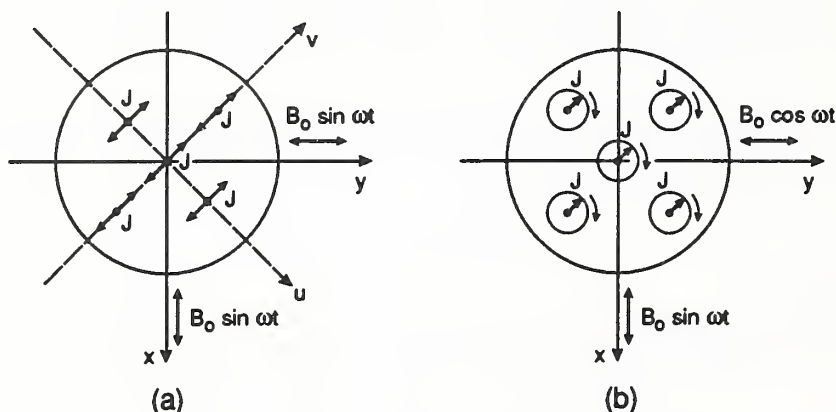


Figure 2. (a) Induced current sheet oscillates along fixed direction for linearly polarized magnetic field (b) induced current sheet rotates with constant magnitude for circularly polarized magnetic field.

It is noted that the root mean square (rms) value of J_l is equal to the rms value of J_o .

Thus, when the applied magnetic field is linearly polarized, cells plated on the bottom surface of a culture vessel and which are away from the edges of the vessel will be exposed to a sheet of current that oscillates in magnitude [Eq. (4)] along a fixed direction indicated by the J vectors shown in Fig. 2a. In contrast, when the applied magnetic field is circularly polarized, cells experience a current sheet, constant in magnitude, that never "turns off" [Eq. (5)] and that rotates 360 degrees about the z-axis for every cycle of the applied magnetic field. The rotating nature of the current sheet can be inferred from the rotating J vectors shown in Fig. 2b. In addition, the peak value of the current induced by the linearly polarized magnetic field is 41% greater than for the circularly polarized case, i.e., J_l (peak)/ J_o is equal to $\sqrt{2}$. Similar observations are true for the induced electric fields, \vec{E} , experienced by the cells because \vec{J} is equal to $\sigma \vec{E}$. The fact that the induced electric field does not pass through zero for the circularly polarized case may have relevance if a resonance model is being tested.

An approximate expression for the rate of energy deposition near the bottom (or top) surface of the culture medium is developed next. The rate that energy is deposited in the culture medium, $\dot{\epsilon}$, is given by the product, $I^2 R$, where I is the current near the bottom surface and R is the electrical resistance offered by the culture medium. As for the induced current and electric field, $\dot{\epsilon}$ will be very small compared to its naturally occurring counterpart in a biological system.

We consider first a current I_u through a small cross sectional area dA_u close to the bottom of the culture medium at some instant. This current can be expressed as

$$I_u = \vec{J} \cdot d\vec{A}_u \quad (6)$$

where $d\vec{A}_u$ is a vector parallel to \vec{J} and has magnitude dA_u , i.e.,

$$d\vec{A}_u = dA_u \frac{J_x \hat{i} + J_y \hat{j}}{\sqrt{J_x^2 + J_y^2}}.$$

Thus, I_u is just

$$I_u = dA_u \sqrt{J_x^2 + J_y^2}. \quad (7)$$

The resistance, R_u , encountered by this current is approximately

$$R_u \simeq \frac{L_u}{\sigma dA_u}, \quad (8)$$

where L_u is the distance across the bottom surface (L_u does not actually extend completely across the surface because J vanishes at the perimeter as shown in Fig. 1b). Therefore, the rate that energy is deposited along a narrow path parallel to \vec{J} is

$$d\dot{\epsilon} \simeq I_u^2 R_u = \frac{dA_u}{\sigma} (J_x^2 + J_y^2) L_u \quad (9)$$

To obtain an approximate expression for the total rate of energy deposition, we make use of the dashed coordinate system u, v shown in Fig. 2a. The cross sectional area, dA_u , along the u -axis is taken to be $z_o du$ where z_o is a very small length in the z direction and du is an element of length along the u -axis. For a given value of u , L_u extends from $-\sqrt{a^2 - u^2}$ to $\sqrt{a^2 - u^2}$ or is equal to $2\sqrt{a^2 - u^2}$. Therefore,

$$d\dot{\epsilon}_u \simeq \frac{2z_o}{\sigma} (J_x^2 + J_y^2) \sqrt{a^2 - u^2} du \quad (10)$$

The total $\dot{\epsilon}$ for $-a < u < a$ is then

$$\dot{\epsilon} = \int_{-a}^a d\dot{\epsilon} \simeq \frac{z_o \pi a^2}{\sigma} (J_x^2 + J_y^2) \quad (11)$$

From Eqs. (4, 5 and 11), we have for a linearly polarized magnetic field that

$$\dot{\epsilon}_l \simeq \frac{z_o \pi a^2 C^2}{\sigma} 2B_o^2 \sin^2 \omega t = \frac{z_o \pi a^2 C^2}{\sigma} B_o^2 (1 - \cos 2\omega t), \quad (12)$$

and for a circularly polarized magnetic field,

$$\dot{\epsilon}_o \simeq \frac{z_o \pi a^2 C^2}{\sigma} B_o^2. \quad (13)$$

Eqs. (12 and 13) indicate that the rate energy is deposited by the linearly polarized magnetic field pulsates at twice the frequency of the applied field and the peak rate is twice as large as the nonpulsating $\dot{\epsilon}_o$ produced by the circularly polarized magnetic field. It is noted that the average value of $\dot{\epsilon}_l$ is equal to $\dot{\epsilon}_o$. Most of the above results extend to in vitro studies with culture vessels that are square or rectangular

in geometry. However, the calculation of $\dot{\epsilon}$ for a circularly polarized magnetic field is more difficult because R changes in a complicated way as \vec{J} rotates.

In summary, when comparing the induction effects of circularly and linearly polarized magnetic fields for the experimental geometry chosen, the following observations can be made: the maximum J or E that most cells are exposed to will be 41% greater when the magnetic field is linearly polarized; J and E will oscillate along a fixed direction (passing through zero) when B is linearly polarized; J and E rotate with constant magnitude (never vanishing) when B is circularly polarized; the rms values of J (or E) are equal regardless of polarization; $\dot{\epsilon}$ will pulsate twice every cycle and the maximum value of $\dot{\epsilon}$ will be twice as large when B is linearly polarized; $\dot{\epsilon}$ remains constant when B is circularly polarized but the average values of $\dot{\epsilon}$ are equal regardless of polarization. The significance of the differences, if any, is unknown.

1.3 Measurements of Ion Mobility at Hydro-Quebec

At the request of researchers at Hydro-Quebec, measurements of time-of-flight (TOF) air ion spectra were performed in an exposure system using a NIST-developed pulse TOF drift tube [4]. The exposure system is designed to generate dc electric fields with positive ions. Ions are produced by wires that are set into corona and the ions are guided with electric fields into a room 5 m \times 5 m \times 3 m high. The ceiling of the room is a metal screen (through which the ions enter) and the floor is metal plate covered with partially conducting carpet. Except for size and the use of walls with guard bands, the electrical design is similar to the NIST parallel plate apparatus developed in 1980 to check the performance of dc electric field meters, Wilson plates, and aspirator type ion counters [5–7]. Electric field meters and Wilson plates (for current density measurements) were located near the floor of the exposure system and the NIST drift tube was positioned about 50 cm above the floor.

Fig. 3 shows TOF spectra of positive ions measured at different times over two days. The electric field strength (E) and ion current density (J) near the floor were held fixed and were approximately 30 kV/m and 0.18 $\mu\text{A}/\text{m}^2$ respectively, for all the spectra. The top trace in Fig. 3 shows three resolved peaks (a,b,c) on March 12. Not much change is apparent during the observation on the following morning, but by early afternoon (13:32 hr), a new peak (d) has appeared. Later in the afternoon (14:55 hr), feature (b) has decreased in relative abundance and is now less abundant than (d).

Fig. 4 shows that the distribution of ion species can be changed by varying the electric field and current density in the exposure chamber. The top trace in Fig. 4 is the same as the bottom trace of Fig. 3. The lower trace in Fig. 4 shows the change in TOF spectra when E and J are increased to approximately 43 kV/m and 0.28 $\mu\text{A}/\text{m}^2$, respectively.

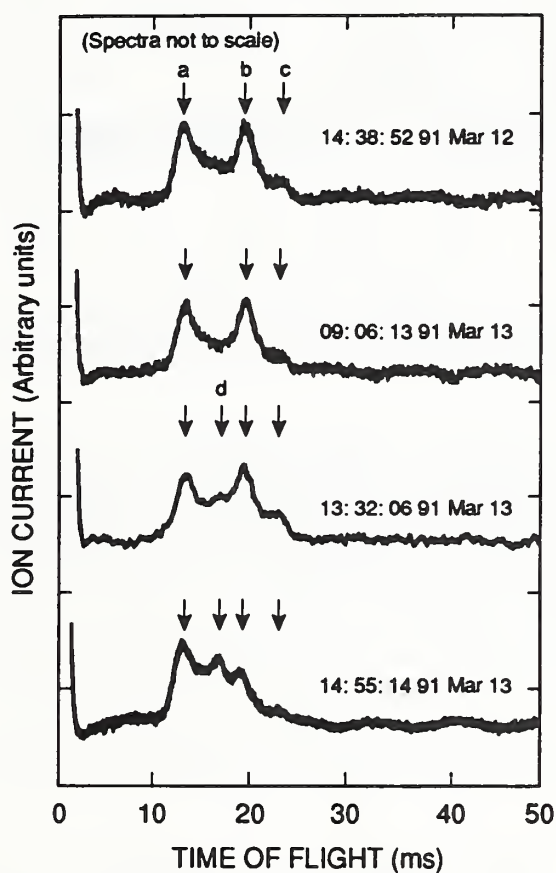


Figure 3. Time-of-flight spectra for positive ions in IREQ exposure system as function of time over period of two days. The appearance of feature d in the afternoon of the 2nd day and the changes in relative abundances reflects changes in air composition.

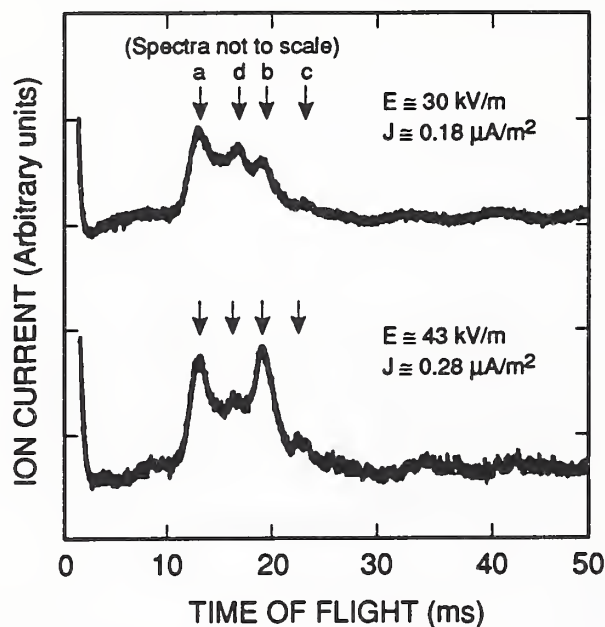


Figure 4. Time-of-flight spectra in IREQ exposure system for different electric fields and current densities.

No attempt was made to control the temperature or relative humidity, which ranged from 21.8 to 22.9 degrees Celsius and 26.0 % to 30.4 %, respectively. The air pressure was near 101.7 kPa. The electric field strength in the drift tube was 24.8 kV/m and, for the spectra in Figs. 3 and 4, the ions traveled a distance of 4 cm in the drift tube. Ions entered the drift tube by pulsing open a shutter for 0.9 ms. The ion number density near the floor of the exposure system for the data in Figs. 3 and 4 was estimated to be between 3 and 4×10^5 ions/cm³. An air handling system for the exposure system was not operated during the measurements. The operation of the drift tube is described in detail in Ref. [4]. Use of a signal averager is required for processing the ion current signal from the drift tube.

The mobility values of peaks (a) and (b) in the figures are 1.41×10^{-4} and 0.96×10^{-4} m²/Vs, respectively. These values are free of so called “end effects” of the drift tube [4] because TOF spectra were measured with both 4 cm and 8 cm path lengths to determine the correct time-of-flight of peaks (a) and (b). The uncertainty in the mobility value of (a) is estimated to be less than $\pm 2\%$. A larger uncertainty, $\pm 5\%$, is associated with peak (b) because the peak position of (b) is affected more by overlapping from adjacent peaks. It should be noted that there is likely to be more than one ion species forming a single TOF peak, i.e., there can be several ion species with nearly the same mobility [8].

The mobility measurements at Hydro-Quebec are of interest for a number of reasons:

-
- Because of the temporal changes in ion composition, as indicated by changes in TOF or mobility spectra, and the possible influence of ion species on the outcome of a biological study with dc electric fields and ions, a case can be made for requiring the conditioning of laboratory air (e.g., use of different filters) so that the composition of the ions remain constant during the course of the study. Ion mobility spectrometry with relatively simple drift tubes can be used to measure the mobility spectra of the ions as an approximate check of the constancy of the ion composition. (Ideally, it would be desirable to monitor the ion masses using a mass spectrometer, but because of cost considerations and the added complexity of operating a mass spectrometer in combination with an exposure system, use of a mass spectrometer will not be practical in most cases.) A minimum requirement when comparing the results of laboratory studies from different laboratories would be that mobility spectra be the same in both laboratories.
 - The mobility measurements described above are the first of their kind in a biological exposure system, and the first conducted by NIST outside its own facility. The planned Hydro-Quebec study (perception thresholds for sensing dc electric fields with ions) will also be a “first” when undertaken.
 - The charge densities in the exposure system were 4 to 5 times lower than in the NIST apparatus used for producing air ions. With signal averaging, it was possible to obtain TOF spectra of the ions with adequate resolution to identify the positions of the major ion peaks and changes in TOF spectra as a function of time.

2 GASEOUS DIELECTRICS RESEARCH

Task 02

Richard J. Van Brunt, James K. Olthoff and Kenneth L. Stricklett
Electricity Division
National Institute of Standards and Technology

John T. Herron
Chemical Kinetics Division
National Institute of Standards and Technology

Manish Shah
Harvard University Medical School
Cambridge, MA 02138

H.-X. Wan and J. H. Moore
Department of Chemistry and Biochemistry
University of Maryland
College Park, MD 20742

2.1 Introduction

The objectives of this project are the development of measurement capabilities and the providing of fundamental data as part of the Department of Energy's basic research concerned with the development and evaluation of advanced compressed-gas-insulation technology.

To reduce space requirements and improve the efficiency of high-voltage transmission systems, the electric power industry has turned toward more extensive use of compressed-gas insulation. To design meaningful tests of system performance and establish specifications for the quality of materials used in such systems, more information is needed about the fundamental physical and chemical processes which lead to insulation deterioration and electrical breakdown. The research includes applications of gas chromatography-mass spectrometry to characterize corona discharge by-products; and the acquisition of fundamental data, such as, reaction-rate coefficients, corona-inception voltages, production rates of corona by-products, the effects of contaminants on discharge initiation, and the rates of discharge-induced decomposition of the gas.

This section of the report highlights progress of research in two areas related to the decomposition of SF₆ in electrical discharges. The first is concerned with the production of S₂F₁₀ in corona discharges. Using a mass spectrometer-gas chromatograph capable of detecting S₂F₁₀ concentrations in SF₆ down to the part in

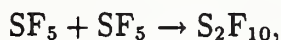
10⁹ level, the rates of S₂F₁₀ production from dc glow-type negative point-plane corona discharges in pressurized SF₆ have been measured at different absolute gas pressures in the range of 100 to 500 kPa (1 to 5 atm) and at different constant discharge currents in the range 2 to 80 μA. The charge rate-of-production for S₂F₁₀ is observed to drop with decreasing discharge current and the yield curves exhibit nonlinearities in the early stages of the discharge that appear to be associated with “conditioning” of the point electrode. The nonlinearities become more pronounced with increasing gas pressure. The results are found to be quite reproducible and suggest the possibility of using this type of corona discharge as a reliable method for preparing reference gas samples that contain predictable trace quantities of S₂F₁₀ in SF₆.

The second area of research is concerned with the measurement of fundamental electron scattering and dissociative electron attachment cross sections for SF₆ and its electrical-discharge by-products. Absolute, total electron scattering cross sections for 0.2–12 eV electrons on SF₆, SO₂, SOF₂, SO₂F₂, SOF₄, and SF₄, as well as cross sections for negative-ion formation by attachment of 0.2–8 eV electrons have been measured. These cross sections are used to calculate dissociative-attachment rate coefficients as a function of E/N for SF₆ by-products in SF₆.

2.2 Rate of S₂F₁₀ Production from Negative Corona in Compressed SF₆

2.2.1 Introduction

Disulfur decafluoride (S₂F₁₀) is now known to be formed when electrical discharges occur in compressed sulfur hexafluoride (SF₆) commonly used as a gaseous dielectric in high-voltage apparatus [9, 10]. The possible presence of this compound in SF₆ is of concern because it is known to be highly toxic [11]. The primary mechanism for its formation is believed to be the reaction



where SF₅ is formed by collisional dissociation of SF₆ in the discharge and the above reaction involves stabilization via interaction with a third body. Since S₂F₁₀ is thermally unstable above about 150°C [12], it tends to form only in the “cold” regions of the discharge. Favorable conditions for its production thus exist in low-level negative glow-type corona discharges in which there is no significant heating of the gas.

In the normal operation of SF₆-insulated power equipment, it can be expected that internal corona or partial discharges will occur that cause decomposition of the gas.

It is therefore desirable to know the rates for S_2F_{10} production under these conditions in order to determine gas toxicity levels and assess possible hazards associated with exposure to decomposed SF_6 .

The dc point-plane negative glow corona in SF_6 is a constant-current discharge that is easily controlled and amenable to theoretical chemical kinetics modelling [13,14]. It shows promise as a type of reference discharge capable of generating gas samples containing known trace quantities of S_2F_{10} in SF_6 suitable for calibration of analytical detection methods. The ability to quickly produce reliable reference gas samples in the laboratory is especially desirable in the case of S_2F_{10} for two reasons: 1) it eliminates the necessity of dealing with pure S_2F_{10} which requires special procedures because of its high toxicity, and 2) it avoids the problems associated with long-term decomposition of S_2F_{10} in gas sample cylinders noted in previous work [15,16].

Before serious consideration can be given to the use of a negative corona for preparing S_2F_{10} reference samples, more must be known about the factors that affect S_2F_{10} yield in such discharges. Information is needed about how S_2F_{10} production rates are influenced by changes in such parameters as discharge current, gas pressure, and the initial purity of the SF_6 . Effects of electrode geometry, material, and surface conditions must also be evaluated. Attention should be given to the formation of gaseous by-products that can interfere with the detection of S_2F_{10} in SF_6 , e.g., SOF_4 , S_2OF_{10} , and $S_2O_2F_{10}$.

The present work represents a step toward acquisition of the information required to determine the reliability of using a negative point-plane corona to generate known trace quantities of S_2F_{10} in SF_6 . The dependencies of measured S_2F_{10} yields on discharge current, gas pressure, and preconditioning of electrodes are reported here.

2.2.2 Measurement Method

The measurement procedures used to obtain the data reported here are similar to those described previously to investigate the decomposition of SF_6 in corona discharges [10,17]. The discharges were generated in a 3.7 liter cell at room temperature using stainless-steel electrodes with a point-to-plane gap spacing of 1.0 cm and a point tip radius-of-curvature of about 0.08 mm. Most of the data reported here were obtained with electrodes that were initially both polished and cleaned. For some measurements, as noted below, point electrodes were preconditioned by using them to generate a negative corona in SF_6 for several hours. These electrodes were then cleaned, but not polished, prior to use in an experiment.

A previously described analytical technique [16] employing a gas chromatograph-mass spectrometer (GC/MS) was used to measure the S_2F_{10} content in SF_6 . The GC/MS configuration is shown in Fig. 5. Gas samples extracted from the discharge region of the corona test cell with a gas-tight syringe are injected into the GC-column. After

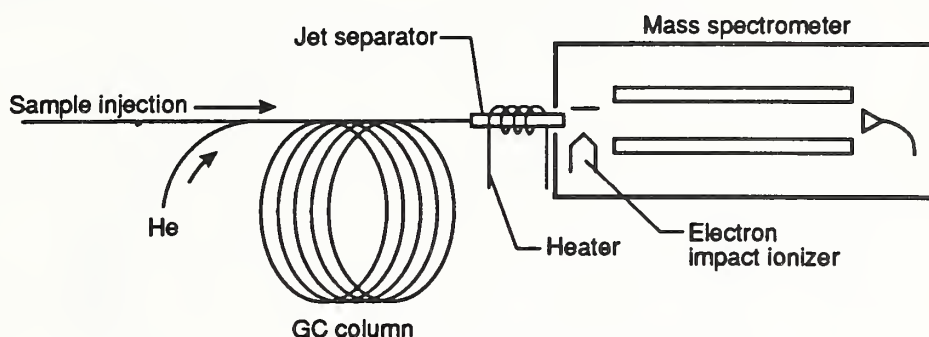


Figure 5. Gas chromatograph mass spectrometer system used to detect S_2F_{10} in SF_6 [8]. S_2F_{10} is converted to SOF_2 in the heated jet separator.

passing through the column, the S_2F_{10} is converted to SOF_2 by reaction with water adsorbed on the surface of a jet separator heated to a temperature of about $180^\circ C$. The SOF_2 formed by this process is ionized by electron impact and detected with a quadrupole mass spectrometer tuned to select ions with a mass-to-charge ratio (m/e) of 86 corresponding to SOF_2^+ . This method achieves a high sensitivity (~ 2 ppb) for detection of S_2F_{10} in SF_6 because it eliminates the background interference from ions associated with SF_6 [16].

Fig. 6 shows an example of a GC/MS single-ion chromatogram for $m/e = 86$ used to determine the quantity of S_2F_{10} generated by a corona discharge in SF_6 . Indicated in this chromatogram are the responses from a typical 30 minute sequence of five individual injections. Two injections from the discharge cell are bracketed by three injections from a reference cell containing a known quantity of S_2F_{10} in SF_6 at the same absolute pressure as the SF_6 in the discharge cell. The samples from the discharge cell exhibit peaks associated with SOF_2 that was produced in the discharge. These peaks are not present in the reference samples. The SOF_2 peak in the discharge sample is well separated in time from the S_2F_{10} peak and causes no interference at these concentrations.

The S_2F_{10} concentrations were determined by comparing the areas under the peaks for the discharge samples with those for the reference samples. At present, the largest source of error in the measurement of S_2F_{10} concentrations is associated with uncertainties in the reference sample concentrations. Other errors result from systematic changes in the GC/MS response to S_2F_{10} following each successive injection; presumably due to conditioning effects from depletion of adsorbed H_2O in the jet separator. The method indicated in Fig. 6 of bracketing injections allows assessment of this source of error.

It should finally be noted that the injection sequence, as shown in Fig. 6, is programmed to turn off the mass spectrometer during those times when SF_6 elutes from the column, e.g., between 0 and 2.2 minutes. This is necessary to reduce the background and avoid overstressing the ion detector.

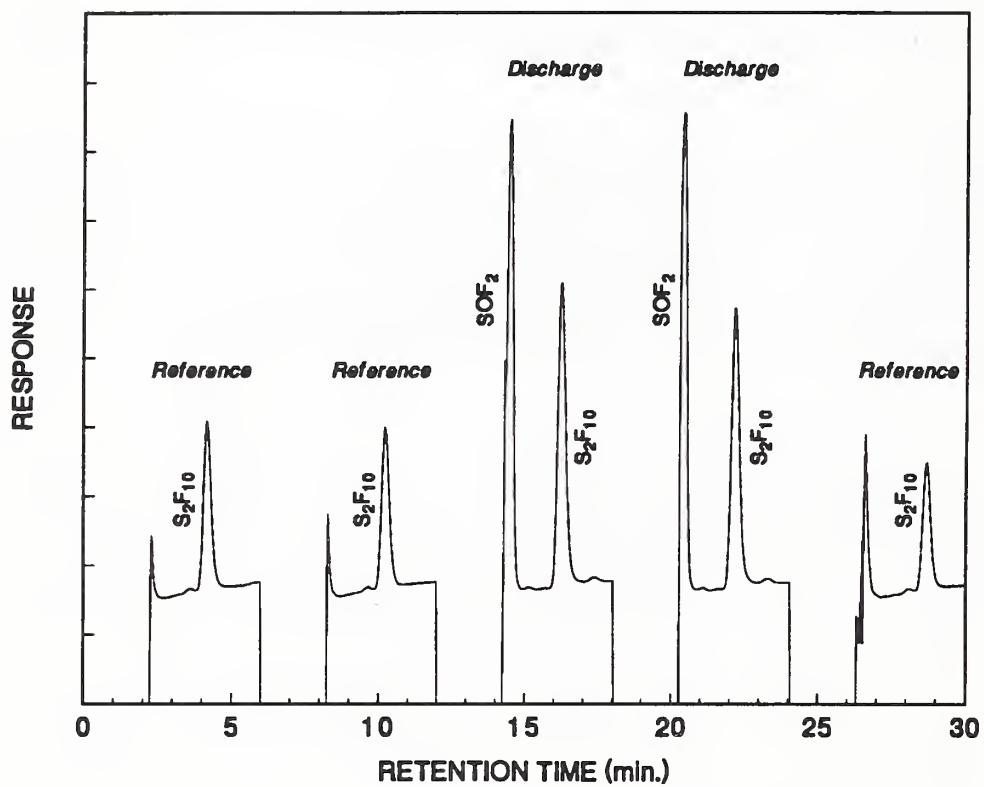


Figure 6. Single-ion chromatogram at $m/e = 86$ for a typical injection sequence showing three injections from a reference cell and two from a corona discharge cell. Peaks associated with SOF_2 and S_2F_{10} are indicated.

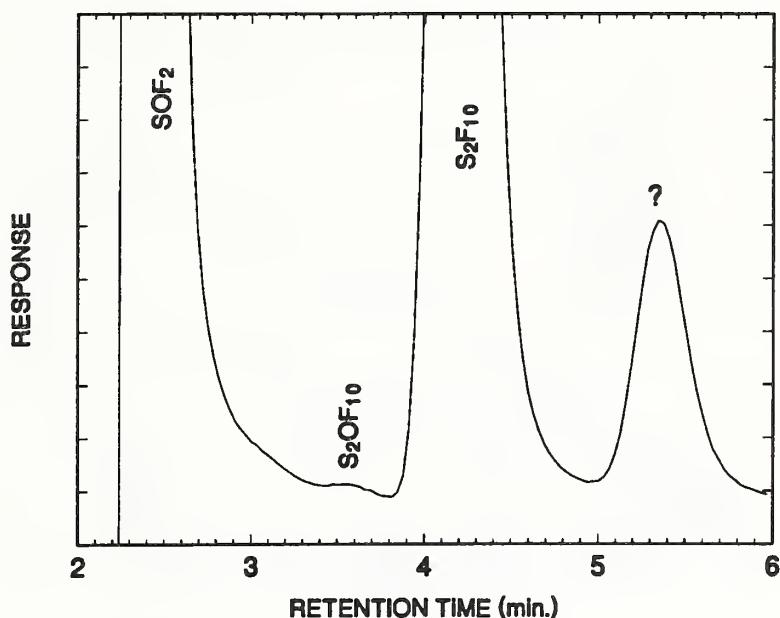


Figure 7. Blow-up of a single-ion chromatogram at $m/e = 86$ indicating features associated with SOF_2 , S_2OF_{10} , and S_2F_{10} . The peak designated with a question mark is presently unknown, but is suspected to be $S_2O_2F_{10}$.

2.2.3 Results

Fig. 7 shows a blow-up of a chromatogram at $m/e = 86$ corresponding to a single injection from the discharge cell. This chromatogram shows features associated with SOF_2 , S_2OF_{10} , S_2F_{10} and an unknown species, indicated by the question mark, which is tentatively identified as $S_2O_2F_{10}$. The presence of S_2OF_{10} and $S_2O_2F_{10}$ is of particular concern because these species are reported to have column retention times close to that of S_2F_{10} [18] and because they can produce SOF_2^+ by collision with electrons in the ionizer of the mass spectrometer. These species thus appear in the $m/e = 86$ chromatogram and may interfere with the detection of S_2F_{10} by the method used here. The data in Fig. 7 indicate that the features associated with the different species that appear at $m/e = 86$ are sufficiently well separated under the operating conditions used to avoid significant interference effects. It should be noted that the peaks identified here with S_2OF_{10} and $S_2O_2F_{10}$ always appeared in the decomposed SF_6 for all of the discharge conditions considered in this work.

The measured S_2F_{10} yields in micromoles versus net charge, Q , transported in millicoulombs are shown in Fig. 8 for different discharge currents and for a gas pressure of 200 kPa (≈ 2 atm). The transported charge is given by $Q = It$, where I is the discharge current and t is the time during which the discharge has been operated. The uncertainties in the measured S_2F_{10} yields are estimated to be no more than $\pm 30\%$ in all cases. However, since this uncertainty is due primarily to uncertainties in the reference gas and since the same reference was used for all measurements,

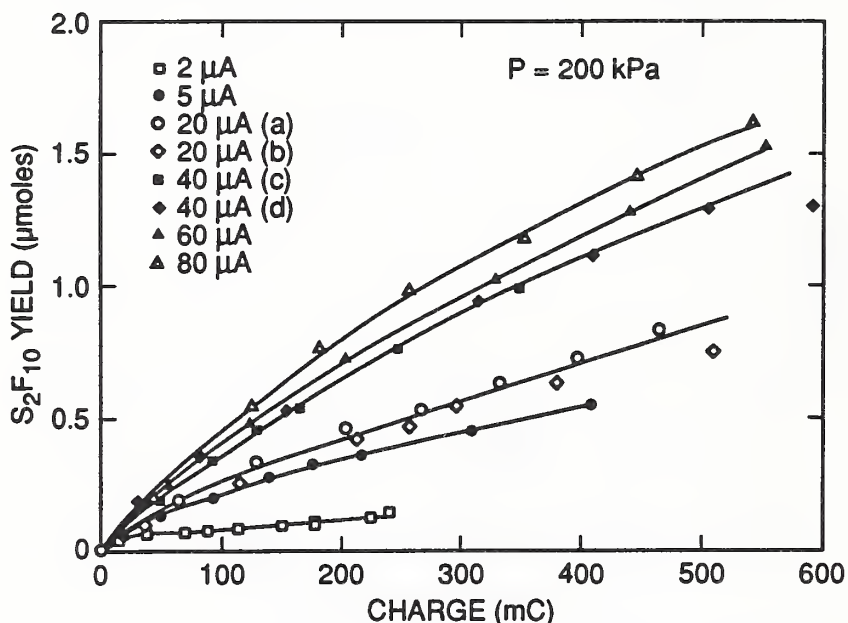


Figure 8. Measured yields of S_2F_{10} versus net charge transported from negative corona discharges in 200 kPa SF_6 at the indicated discharge currents. The data designated (a) and (b) at $20 \mu A$ and (c) and (d) at $40 \mu A$ were obtained from separate experiments performed at different times.

relative reproducibility can be determined with an uncertainty that is much less than implied by uncertainties in absolute yields. The differences between the measured yields obtained for different discharge currents are believed to be significant for the same reason.

The data shown in Fig. 8 indicate that the charge rate-of-production, $d[S_2F_{10}]/dQ$, decreases with decreasing current, especially for $I < 40 \mu A$. This means that the measured time rate-of-production, $d[S_2F_{10}]/dt$, is not directly proportional to the current. However, above $40 \mu A$ the slopes of the $[S_2F_{10}]$ versus Q curves are nearly parallel, thus indicating that $d[S_2F_{10}]/dt$ is approximately proportional to I for $I \geq 40 \mu A$, consistent with preliminary results previously reported [10].

The data obtained from two different experiments performed at widely separated times for both 20 and $40 \mu A$ are seen to be in good agreement thus demonstrating that the results are reproducible and the difference between the S_2F_{10} production rates at these two currents is significant.

The yield curves in Fig. 8 are seen to exhibit significant nonlinearities in the early stages of the discharge, i.e. for $Q < 100$ mC. The rate, $d[S_2F_{10}]/dQ$, is seen to drop significantly from its initial value with increasing Q (or equivalently with increasing time) and eventually approaches a limiting constant value. The initial nonlinear behavior of the S_2F_{10} production is similar to that previously reported for SO_2F_4 production from negative corona in SF_6 [17, 19].

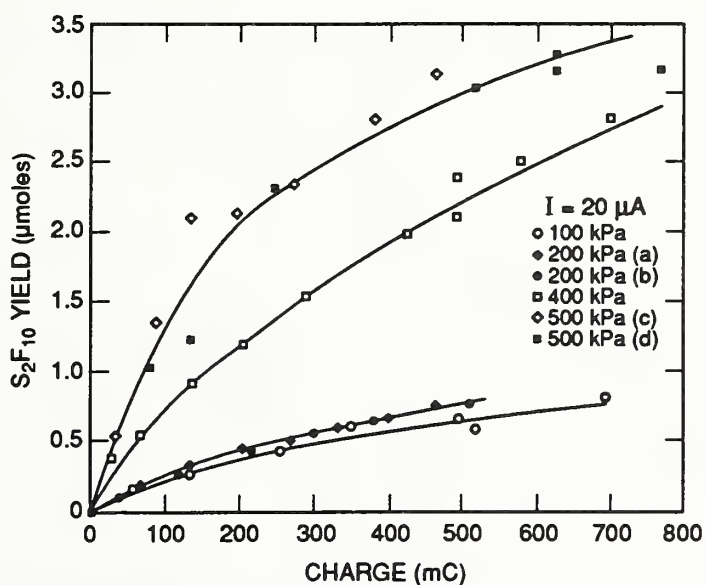


Figure 9. Measured yields of S_2F_{10} versus net charge transported from $20 \mu A$ negative corona discharges in SF_6 at the indicated absolute gas pressures. The data designated (a) and (b) at 200 kPa and (c) and (d) at 500 kPa were obtained from separate experiments performed at different times.

The data for $I = 20 \mu A$ shown in Fig. 9 indicate that the nonlinearities in the S_2F_{10} yield curves become more accentuated as the absolute gas pressure is increased from 100 kPa (1 atm) to 500 kPa (5 atm). There also appears to be a tendency for the limiting S_2F_{10} production rate to increase with increasing pressure. In obtaining the data shown in Fig. 9, it was noticed that the initial rapid increase in $d[S_2F_{10}]/dQ$ was correlated with times during which it was necessary to make significant changes in the discharge gap voltage in order to maintain a constant current. It was then suspected that the observed changes in S_2F_{10} production rate were due at least in part to changes in the discharge behavior or discharge-induced changes in electrode surface conditions.

In an attempt to assess the influence of electrode conditioning on S_2F_{10} production, experiments were performed with electrodes that were preconditioned by using them to generate a corona discharge. The stainless steel point electrodes used to obtain the data in Figs. 8 and 9 were polished before being used in the discharge cell.

It was determined from microscopic observations that a polished point electrode develops a multitude of micro pits or depressions near the tip after being exposed to the discharge. The extent of the pitted region seems to increase slightly with the voltage required to sustain the discharge. The fact that the initial nonlinearities in S_2F_{10} yield become more pronounced with increasing current and gas pressure may be related to corresponding increases in gap voltage.

Fig. 10 shows a comparison between yield curves for a $40 \mu A$ discharge in 400 kPa

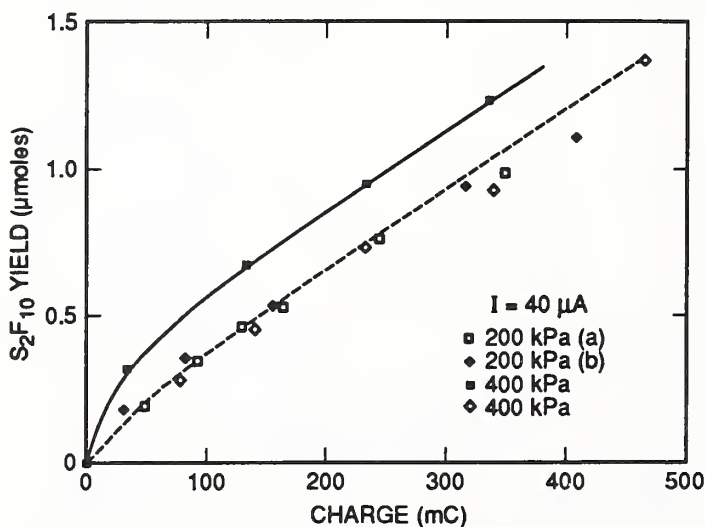


Figure 10. Measured yields of S_2F_{10} versus net charge transported from $40 \mu A$ negative corona discharges in SF_6 at the indicated absolute gas pressures. The data at 400 kPa fitted by a solid line were obtained using a point electrode that was initially polished and the data at 400 kPa fitted by a dashed line were obtained using a preconditioned point electrode. The data designated (a) and (b) at 200 kPa were obtained from separate experiments performed at different times using polished electrodes.

(4 atm) SF_6 that were obtained with and without preconditioning of the point electrode surface. A fit to the 400 kPa data obtained using the preconditioned electrode, as indicated by the dashed line, is seen to agree reasonably well with data from two separate experiments performed at 200 kPa with polished electrodes. It is thus evident from these data that the dependence of S_2F_{10} production on pressure, such as shown in Fig. 9, and the initial degree of nonlinearity are significantly reduced by using preconditioned electrodes.

2.2.4 Discussion and Conclusions

It has been demonstrated from the results presented here that it may be possible to use a negative point-plane glow discharge as a relatively quick method for preparing reliable reference gas samples containing predictable trace levels of S_2F_{10} in pressurized SF_6 . Measured S_2F_{10} yields from corona in SF_6 were found to be quite reproducible. The rates for S_2F_{10} production are found to depend on discharge current, gas pressure, and initial condition of the point-electrode surface.

The S_2F_{10} production rate from discharges generated by point electrodes that were initially polished show a tendency to decrease with time and eventually approach a constant value. This nonlinearity may be partly a consequence of changes in the discharge characteristics with time, e.g., changes in the volume of the glow region. The changes in S_2F_{10} production would tend to decrease as the discharge

stabilizes. Discharge-induced changes in the point-electrode surface may also affect S_2F_{10} production. Local heating and increased surface roughness at the tip of the electrode may enhance surface catalyzed breakup of S_2F_{10} molecules that diffuse to this surface from the nearby discharge volume.

In general, the results reported here yield S_2F_{10} production rates that are lower, by at least a factor of two, than those predicted using a previously proposed chemical kinetics model of the discharge [13, 14]. The model also fails to predict the nonlinearities and pressure and current dependencies reported here. The tendency for the model to over-estimate the S_2F_{10} production rates probably results in part from a failure to include S_2F_{10} destruction mechanisms and processes that compete with S_2F_{10} formation such as could result in production of S_2OF_{10} or $S_2O_2F_{10}$. The initial conditioning of electrode surfaces may be accompanied by an increase in the S_2F_{10} destruction rate on these surfaces. This process could account for the types of nonlinear behavior observed under some conditions with polished electrodes. Moreover, the model includes simplifying assumptions about the discharge characteristics, e.g., the volume of the discharge, that simply may not apply at the lowest discharge currents and highest pressures considered here.

Although S_2OF_{10} , and possibly also $S_2O_2F_{10}$, are always observed together with S_2F_{10} , the mechanisms for formation of these species is not understood. Preliminary measurements made using the present analytical technique showed that the S_2OF_{10} detection sensitivity is relatively low compared with S_2F_{10} and therefore the S_2OF_{10} concentration in SF_6 decomposed by corona may be considerably greater than suggested by the response seen in Fig. 7.

2.3 Electron Scattering and Dissociative Attachment

2.3.1 Introduction

An understanding of the physical processes occurring in SF_6 discharges requires a knowledge of the manner in which electrons interact with the decomposition by-products of SF_6 . Cross sections and rate coefficients for such interactions are essential for the modeling of SF_6 electrical-discharge chemistry. A dearth of such information has led us to undertake measurements of absolute cross sections for total electron scattering and for negative-ion formation through electron attachment to SF_6 and to SO_2 , SOF_2 , SO_2F_2 , SOF_4 , and SF_4 , all of which are commonly produced in electrical discharges in SF_6 . These results are compared with previous cross section measurements (where available) and with mass-spectrometric studies for ion identification. Dissociative attachment rate coefficients for the SF_6 decomposition products in SF_6 are calculated as a function of electric field-to-gas density ratio (E/N) using the cross sections reported here. The range of E/N values considered here is that which applies to electrical-discharge conditions.

2.3.2 Experiment

An electron transmission spectrometer employing a trochoidal monochromator [20] forms the basis of the experimental apparatus. This instrument consists of a thermionic electron source followed by the trochoidal monochromator, an accelerating lens, a gas cell, and a retarding lens which permits only unscattered electrons to be transmitted to an electron collector. The instrument is immersed in a uniform magnetic field of about 7 mT (70 gauss). The electron energy resolution was set to about 100 meV and the temperature within the scattering region was maintained at 328 K. The energy scale was calibrated by observing the vibrational structure of the Π shape resonance in N_2 and has an uncertainty of < 50 meV. Total electron-scattering cross sections are obtained by measuring the attenuation of the transmitted current due to the introduction of a sample into the gas cell [21]. Cross sections for electron attachment yielding metastable negative ions (lifetimes $> 10 \mu\text{s}$) and dissociative-attachment processes are determined from a measurement of the resulting negative ion flux to the walls of the gas cell [22]. More detailed experimental descriptions have been published elsewhere [21, 22].

The presence of the magnetic field introduces uncertainty in the length of the electron trajectories through the gas cell [21] as well as uncertainty in the acceptance angle defined by the retarding lens which precedes the collector [23]. Additional uncertainty is associated with the measurement of the target gas pressure in the 0.03 to 0.13 Pa (0.2 to 1.0 mtorr) range at which the cross sections were determined. Overall, the cross sections reported are believed to be accurate to within $\pm 15\%$ for electron energies above 1 eV. Below this energy, the uncertainty may increase to as much as $\pm 50\%$ at the lowest energies (≤ 0.2 eV). Measurement of cross sections for well characterized gases, such as N_2 and N_2O , indicate that discrepancies between values obtained with this technique and other previously reported values are less than these estimated uncertainties. Due to adverse interactions of the sulfur-containing compounds with the electron source, the limit of sensitivity in the dissociative-attachment cross section measurements is about $2 \times 10^{-18} \text{ cm}^2$.

The SF_6 , SO_2 , SOF_2 , and SO_2F_2 samples were obtained from commercial sources and were used without further purification. The SOF_4 and SF_4 samples were prepared by Dr. D. DeMarteau (Clemson University) with stated purities of $> 99\%$. The purities of all samples were checked by mass spectrometry and GC/MS.

2.3.3 Experimental Results and Discussion

SF_6

The present measurement of the total electron-scattering cross section for SF_6 is shown in Fig. 11 and is compared with previous measurements [24–26]. Above 0.5 eV all of the measurements agree to within 10%. Below 0.5 eV the values from the

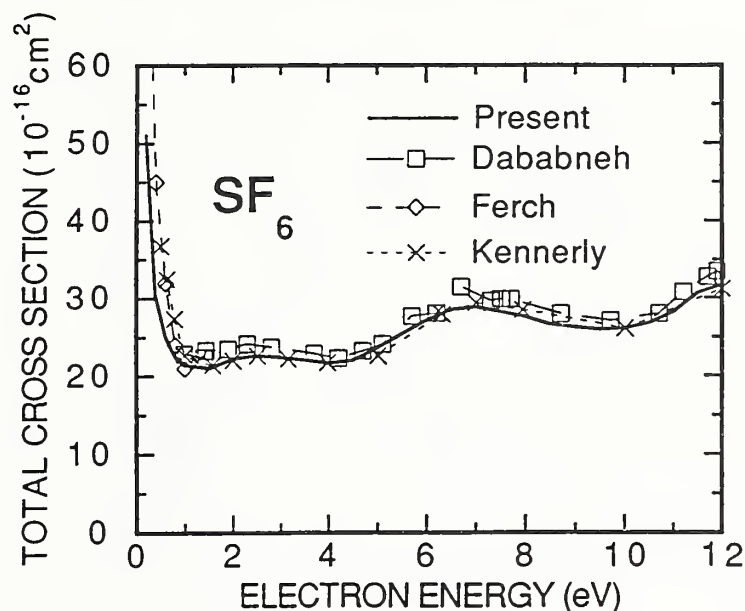


Figure 11. Total electron-scattering cross sections for SF_6 as measured by the present experiment compared with previous measurements by Dababneh *et al.*, (Ref. 17), Ferch *et al.* (Ref. 18), and Kennerly *et al.* (Ref. 16).

present work fall systematically below the cross sections reported by Kennerly *et al.* [24] and Ferch *et al.* [26]. This may be due to the use in this experiment of a retarding potential filter to reject scattered electrons. The acceptance angle of a retarding potential filter increases with decreasing energy most markedly at very low energies.

Negative-ion formation by electron attachment and dissociative attachment to SF_6 has been the subject of intensive study [27, 28]. Christophorou and co-workers have performed several swarm studies [29] of electron attachment to SF_6 , and Fenzloff *et al.* [30] have published a detailed study of the relative ion yields for dissociative attachment to SF_6 . At very low energies (0 – 2 meV), Chutjian and co-workers [31] have measured absolute attachment cross sections using threshold photoemission as an electron source. Kline and co-workers [32] have measured cross sections for attachment and dissociative attachment to SF_6 from 0.01 eV to 15 eV in a beam experiment where the absolute magnitudes were determined by measuring the various positive-ion cross sections and calibrating to total ionization cross-section measurements [33]. More recently, Hunter and co-workers [34] have calculated cross sections for attachment and dissociative attachment to SF_6 using attachment rates measured in swarm experiments in extremely diluted mixtures of SF_6 in N_2 , Ar, and Xe. Differences between the dissociative attachment cross section measurements exceed an order of magnitude.

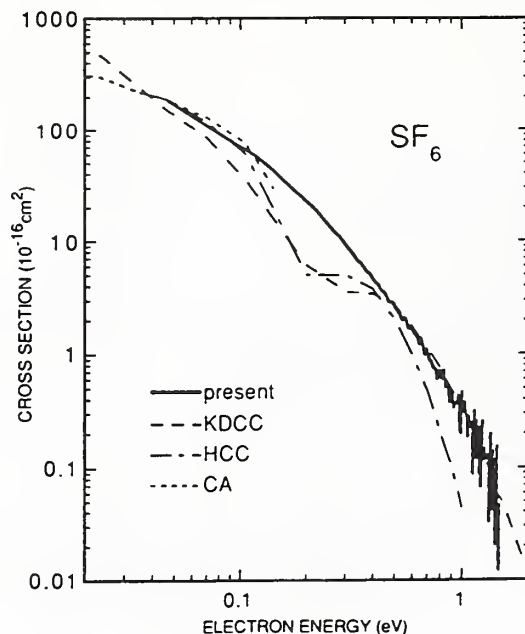


Figure 12. Cross sections for attachment and dissociative attachment to SF_6 as compared with previous measurements by Kline, Davis, Chen and Chantry (Ref. 32), Hunter, Carter, and Christophorou (Ref. 34), and Chutjian and Alajajian (Ref. 31).

The combined cross section for electron attachment and dissociative attachment to SF_6 is measured in the present experiment for electron energies from 0.04 eV to 1.1 eV (Fig. 12). For electron energies less than 0.2 eV, electron attachment is dominated by SF_6^- formation, and above 0.2 eV, by SF_5^- formation from dissociative attachment [30]. The sum of the attachment and dissociative-attachment cross sections as measured by Kline *et al.* [32] and by Hunter *et al.* [34] are shown for comparison in Fig. 12. The cross section for electron attachment at low energies (< 0.2 eV) as measured by Chutjian and coworkers [31] is also shown. The cross section values from the present work are in reasonable agreement with previous measurements for energies less than 0.1 eV and are also in apparent agreement with Kline *et al.* [34] for electron energies exceeding 0.4 eV. However, for intermediate energies ranging from 0.1 to 0.4 eV, the cross sections from the present work significantly exceed those published previously [32, 34].

The apparent discrepancy from 0.1 to 0.4 eV between the present data and the previously published cross sections [32, 34] may be explained by the differences in the experimental detection procedures. In the present experiment, most ions are detected less than 0.5 cm from the point of formation corresponding to a time from formation of less than 10 μs . This allows for the collection of SF_6^- ions that are formed in excited states with relatively short lifetimes. Evidence suggests that these lifetimes range in length from a few microseconds to milliseconds [35]. Ions formed in excited states of SF_6^- with short lifetimes may not be detected in the experiment of Kline and coworkers [32] because the mass analysis requires ion transit times longer than

10 μs before detection, resulting in a lower measured effective cross section for SF_6^- formation. In the drift-tube experiment of Hunter *et al.* [34] the detected SF_6^- ions have been collisionally stabilized under relatively high-pressure drift conditions in rare gases. Under these conditions there may also be discrimination against short-lived SF_6^- in excited states. It has been shown [36] that electrons are more readily detached from excited states of SF_6^- by collisions with rare gases, thus destroying those ions before they can be detected in the drift tube.

The lifetimes of excited SF_6^- are expected to decrease with increasing electron energy, so the contribution to the attachment cross section by short-lived ions should be more significant at higher energies. This supports the agreement observed between the cross sections at low energies and the increasing disparity between the measurements for energies exceeding 0.1 eV. A small contribution by short-lived SF_6^- ions to the present measured cross sections for energies above 0.4 eV would indicate that the contribution from SF_5^- ion formation is less than that implied by the SF_5^- dissociative-attachment cross section measured by Kline and coworkers [32]. This is in general agreement with analyses [34, 39–41] of electron swarm data for which it was found necessary to make a downward adjustment in the experimentally determined electron-collision cross sections for SF_5^- in order to obtain attachment coefficients for SF_6 that are in reasonable agreement with results of the most accurate measurements.

SO_2

Three conflicting experimental measurements of the total cross section for electron scattering by sulfur dioxide (SO_2) have been published. These are shown in Fig. 13 along with the measurements from the present experiment. Our results are in closest agreement with the transmission experiment results of Szmytkowski and Maciag [40]. Discrepancies exceeding 20 % are observed at lower energies but are still within the combined estimated uncertainties of the two experiments. Our results are clearly at odds with those of Zubek *et al.* [41], who also employed a transmission experiment, and those of Sokolov and Sokolova [42] who employed an electron cyclotron resonance technique. In addition, we find that the sum of the ionization and elastic scattering cross sections of Orient and co-workers [43, 44] and the electronic excitation cross sections of Vušković and Trajmar [45] falls significantly below our total electron-scattering cross section.

The broad maximum observed in the total cross section near 5 eV corresponds to the second resonance observed by Sanche and Schulz [46] in the derivative electron transmission spectrum. A resonance near 3.4 eV observed by Sanche and Schulz [46] and by Andrić *et al.* [47] is not evident in the total cross section.

As can be seen from the lower curves in Fig. 13, previous measurements of the cross sections for dissociative attachment to SO_2 differ somewhat in magnitude from those reported here. Čadež and co-workers [48] measured total dissociative-attachment cross sections using a transmission experiment similar to that described in this

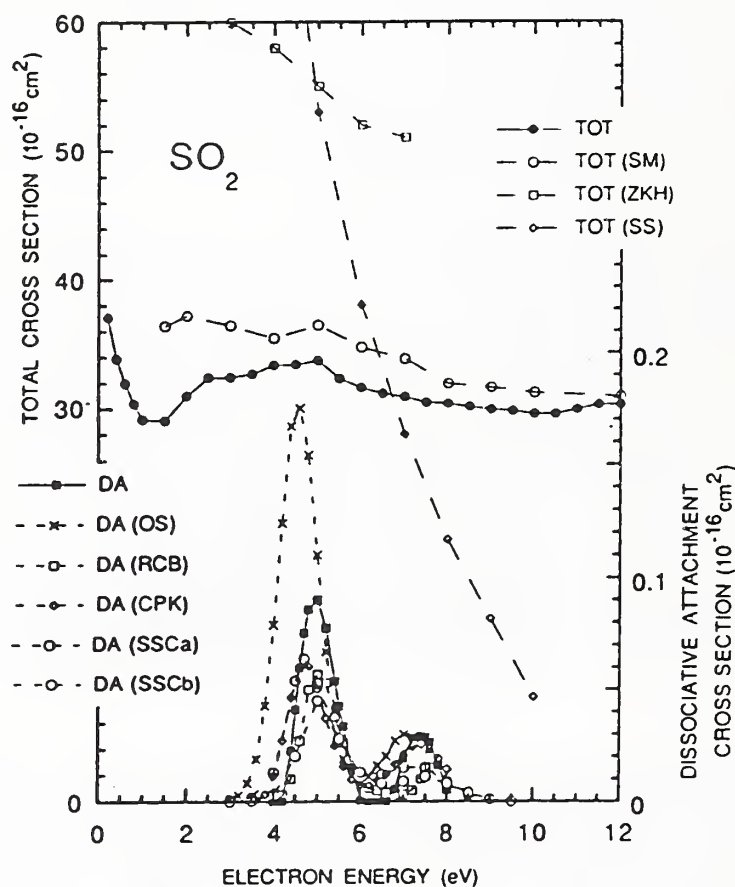


Figure 13. Total electron-scattering cross sections (upper curves, left ordinate) and dissociative attachment cross sections (lower curves, right ordinate) for SO_2 as compared with previous measurements: SM (Ref. 27); ZKH (Ref. 28); SS (Ref. 29); OS (Ref. 31); RCB (Ref. 38); CPK (Ref. 35); SSCa (Ref. 37, time-of-flight measurement); SSCb (Ref. 37; swarm measurement).

paper. Orient and Srivastava [49] measured mass-resolved dissociative-attachment cross sections in a beam experiment with normalization of the measured O^-/SO_2 cross section to the well-known O^-/O_2 cross section. The magnitude of the sum of the mass-resolved cross sections exceeds that of the total cross section measured by Čadež and co-workers [48] by a factor of three. Spyrou *et al.* [50] also carried out a mass-analyzed beam experiment, but determined the magnitude of the cross section by comparison with the production of F^- from C_2F_6 . Their results are in good agreement with Čadež *et al.* In the same paper, Spyrou *et al.* also reported the total dissociative-attachment cross section using a swarm-beam technique which gave magnitudes lower than the beam experiments but in good agreement with early swarm experiments of Rademacher *et al.* [51].

Qualitative agreement between these measurements is good with each experiment showing peaks near 4.7 eV and 7.2 eV with the peak near 4.7 eV corresponding to a broad maximum in the total cross section near 5 eV. The dissociative-attachment cross sections from the present work are within the limits of combined uncertainties when compared with the results of Čadež *et al.* [48] but not when compared with the cross sections of Orient and Srivastava [49]. Spyrou *et al.* [50] have attributed the inconsistencies between the SO_2 dissociative-attachment data of Orient and Srivastava and the other dissociative-attachment measurements to mass-spectrometer discrimination associated with the significant kinetic energy with which O^- is produced in the O^-/O_2 process used for normalization.

Anisotropic angular distributions of the negative-ion fragments formed in the dissociative-attachment process can contribute to inconsistencies between the cross sections measured by different techniques. In general, the negative ions formed by dissociative attachment will exhibit an anisotropic distribution relative to the incident electron beam [52, 53]. The formation of O^- by dissociative attachment of O_2 is known, for example, to exhibit pronounced energy dependent anisotropies [54]. Techniques such as used by Orient and Srivastava [49] that restrict observation of ions to preferred directions relative to the direction of electron motion are most susceptible. In the present experiment, these effects are minimized because all ions are collected.

In recent calculations of excitation energies for transitions of inner-shell electrons to low-lying unfilled orbitals in the sulfur fluorides and oxyfluorides, Tossell [55, 56] has been able to make assignments of the unfilled orbitals involved in the electron capture processes leading to dissociative attachment. These results suggest that the 5 eV resonance in the total cross section and the corresponding dissociation are associated with electron capture into the a_1 orbital of SO_2 , the second-lowest, unfilled molecular orbital.

SOF₂

Total electron-scattering and dissociative-attachment cross sections for thionyl fluoride (SOF_2) are shown in Fig. 14. A prominent resonance in the total cross

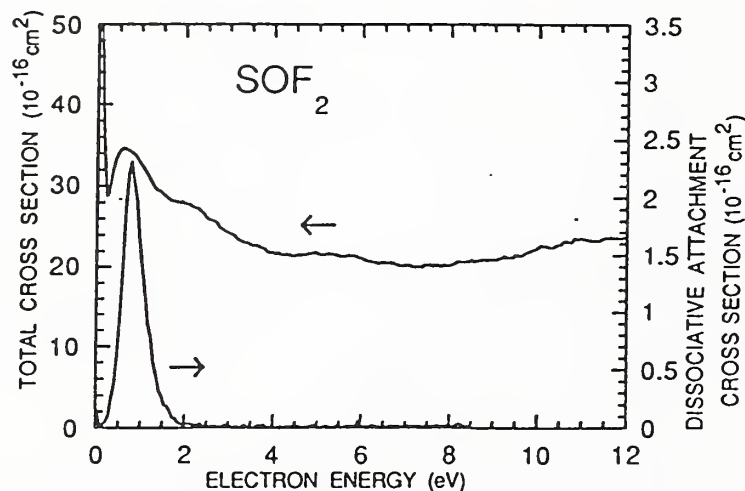


Figure 14. Total electron-scattering (upper curve) and dissociative-attachment (lower curve) cross sections for SOF_2 .

section at 0.6 eV corresponds to a peak in the dissociative-attachment cross section near 0.7 eV. These processes have been assigned to the a'' LUMO state of SOF_2 [55]. A weaker resonance in the total cross section near 2 eV corresponds to a shoulder in the dissociative-attachment cross section near 1.8 eV. Mass-spectrometric studies [57] find an F^- peak near 0.6 eV with a small shoulder near 2 eV in agreement with the present cross sections. For electron energies near 0 eV, Sauers *et al.* [57] have observed the formation of SOF_2^- at peak intensities approximately 200 times smaller than for F^- . This small current would be undetectable in the present experiment.

SO_2F_2

Fig. 15 shows the cross sections for electron scattering and dissociative attachment by sulfuryl fluoride (SO_2F_2). The total cross section exhibits a broad shoulder near 3 eV corresponding to a peak in the dissociative attachment cross section near 3.4 eV. These features have been assigned to the b_1 LUMO state of SO_2F_2 . The peak in the dissociative-attachment cross section near 3.4 eV is in agreement with mass spectrometric studies by Wang and Franklin [58] and by Sauers and co-workers [57]. These studies indicate that this peak corresponds to the formation of SO_2F^- , F_2^- , and F^- , and that the increase in the attachment cross section at low energies is due to the formation of the parent ion, SO_2F_2^- . The dissociative-attachment cross section for room-temperature SO_2F_2 has been calculated from recent electron swarm studies [59] and found to have a peak value of $1.06 \times 10^{-16} \text{ cm}^2$ for 0.22 eV electrons, more than an order-of-magnitude larger than observed in the experiment.

SOF_4

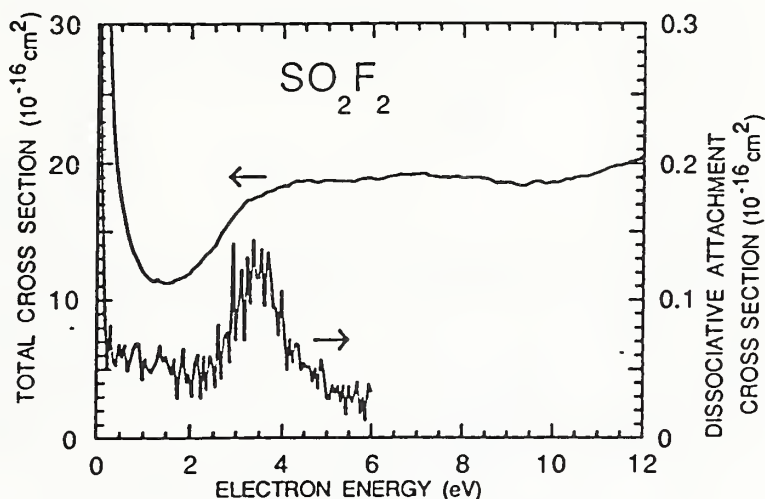


Figure 15. Total electron-scattering (upper curve) and dissociative-attachment (lower curve) cross sections for SO_2F_2 . The increase in the dissociative-attachment cross section at low energies is due to formation of the parent ion SO_2F_2^- .

The total electron scattering and dissociative-attachment cross sections for thionyl tetrafluoride (SOF_4) are shown in Fig. 16. Broad resonance features are observable in the total cross section near 3, 6, and 10 eV. Mass spectrometric studies [57] have identified an F^- peak at 3.2 eV corresponding to the small peak near 3 eV in the dissociative-attachment cross section. The large dissociative-attachment cross section near 0 eV has been shown to correspond to SOF_3^- production [57]. It is of interest to note that the magnitude of the threshold dissociative-attachment cross section for SOF_4 is comparable to the threshold electron-attachment cross section for SF_6 .

SF_4

Total electron scattering and dissociative attachment cross sections for sulfur tetrafluoride (SF_4) are presented in Fig. 17. A strong resonance is observable near 0.4 eV in the total scattering cross section while the dissociative-attachment cross section exhibits a peak at 0.6 eV. These processes are associated with electron capture into the b_2 LUMO of SF_4 [55]. The dissociative attachment peak is in agreement with F^- production observed in previous mass spectrometric data [57]. The increase in the dissociative-attachment cross section at low energies is due to the formation of SF_4^- [57]. Previous studies have determined that the threshold electron-capture cross section for SF_4 is two orders-of-magnitude smaller than for SF_6 [60, 61]. More recent data suggest the threshold attachment rates differ by a factor of 10 [62]. Although we do not go down to threshold, our data indicate that the electron-capture cross sections for SF_4 and SF_6 differ by an order-of-magnitude at 0.2 eV, however it must be noted that only ions with lifetimes greater than 10 μs are detected in our experiment. Since

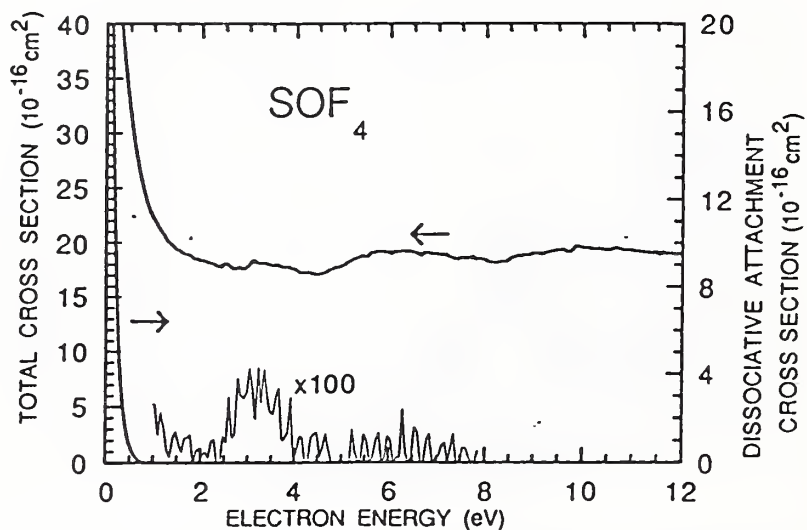


Figure 16. Total electron-scattering (upper curve) and dissociative-attachment (lower curve) cross sections for SOF_4 .

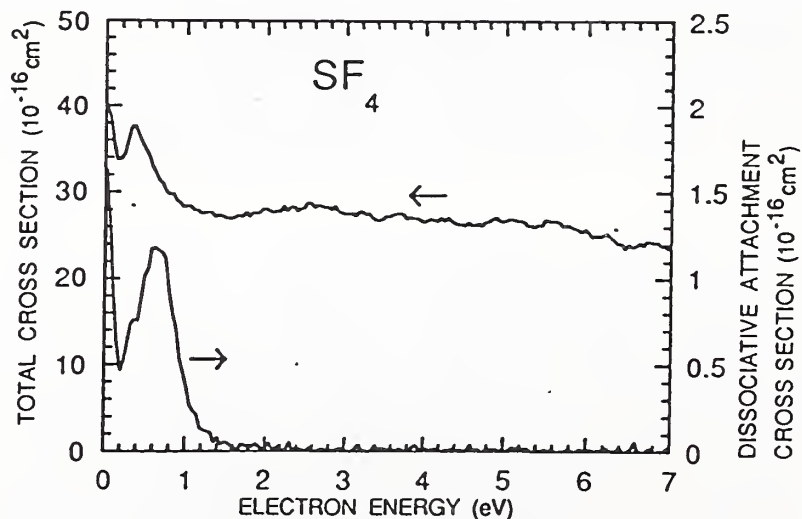


Figure 17. Total electron-scattering (upper curve) and dissociative-attachment (lower curve) cross sections for SF_4 . The increase in the dissociative-attachment cross section at low energies is due to formation of the parent ion (SF_4^-).

the measured lifetime of SF_4^- is in the range of $9.3 \mu\text{s}$ [57] to $16.3 \mu\text{s}$ [60], a significant fraction of the SF_4^- ions can be expected to autodetach before detection.

2.3.4 Dissociative Attachment Rates in SF_6

The dissociate-attachment cross sections for SF_4 , SO_2 , SO_2F_2 , and SOF_2 reported in the previous section have been used to compute dissociative-attachment rate coefficients for these molecules as functions of electric field-to-gas density ratio (E/N) in SF_6 . It was assumed in making the calculations that these species are present at sufficiently low concentrations in SF_6 that one is justified in using electron kinetic-energy distribution functions that apply to pure SF_6 . This assumption is valid in cases where SF_6 is only weakly decomposed in an electrical discharge as occurs in low-level corona or glow discharges [17, 63–65]. It is known from previous calculations [13, 17, 37] that the presence of other electronegative gases in SF_6 below about the 10 percent level has a relatively minor influence on the shape of the electron energy distribution function if E/N is in the range that applies to electrical discharge conditions.

The rate coefficients, k_d , for dissociative attachment were computed using the integral expression

$$k_d(E/N) = (2/m_e)^{\frac{1}{2}} \int_0^\infty \varepsilon f(\varepsilon, E/N) \sigma_d(\varepsilon) d\varepsilon, \quad (14)$$

where ε is the electron kinetic energy, m_e is the mass of the electron, $\sigma_d(\varepsilon)$ is the net dissociative-attachment cross section, and $f(\varepsilon, E/N)$ is the E/N -dependent energy distribution function that satisfies the normalization requirement

$$\int_0^\infty f(\varepsilon, E/N) \varepsilon^{\frac{1}{2}} d\varepsilon = 1. \quad (15)$$

In general, $\sigma_d(\varepsilon)$ corresponds to the sum of all measured dissociative-attachment cross sections of a given molecule for $\varepsilon > 0.2 \text{ eV}$, i.e.,

$$\sigma_d(\varepsilon) = \sum_i \sigma_{di}(\varepsilon), \quad (16)$$

where, in performing the present calculations, the $\sigma_{di}(\varepsilon)$ were represented by Gaussian fits to the measured data corresponding to the different individual features. Dissociative-attachment processes with cross sections peaked at or near zero energy ($\varepsilon < 0.2 \text{ eV}$) were not included in these calculations.

The kinetic energy distributions were computed from numerical solutions to the Boltzmann transport equation using a “two-term” approximation and the set of SF_6 electron collision cross sections proposed by Phelps and Van Brunt [37]. Examples of the computed energy-distribution functions multiplied by the energy, $\varepsilon f(\varepsilon, E/N)$, are

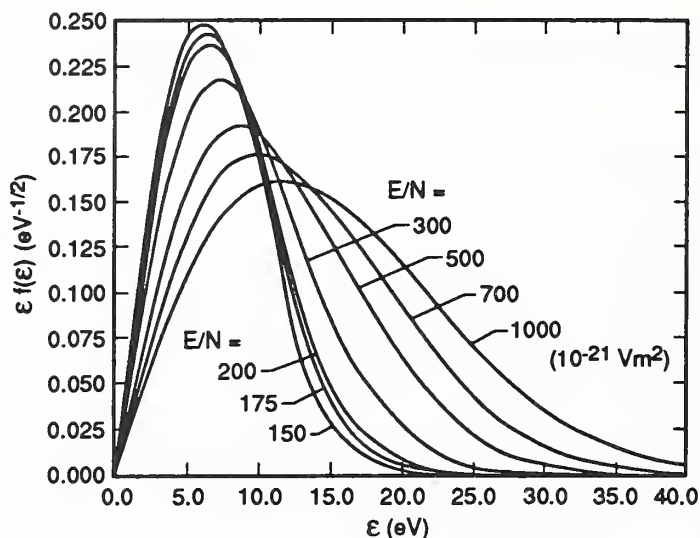


Figure 18. Electron kinetic-energy distribution functions, calculated by the method discussed in Ref. 24, for electrons in pure SF_6 at different values of E/N .

shown in Fig. 18 for E/N in the range of 150×10^{21} to $1000 \times 10^{21} \text{ Vm}^2$. It should be noted that the critical minimum value of E/N required for initiation of a gas discharge in pure SF_6 is $354 \times 10^{21} \text{ Vm}^2$. At this value $\epsilon f(\epsilon, E/N)$ is peaked at about 8.0 eV. Thus, under gas-discharge conditions, it can be expected that dissociative-attachment processes that occur at electron energies above about 1 eV will be relatively more significant to negative-ion formation than processes at lower energies.

The rate coefficients calculated using Eq. (14) are shown in Fig. 19. The results are compared with previously calculated dissociative-attachment rate coefficients for SF_6 which include not only the SF_5^- formation process examined in this work but also the higher energy processes leading to formation of F^- , F_2^- , and SF_4^- [13]. The oxyfluoride rates for the (SOF_2 and SO_2F_2) lie within a factor of two of the SF_6 rate over the E/N range considered. The SO_2 dissociative-attachment rates fall about an order-of-magnitude below the SF_6 rates, as expected, considering the lower cross section. In the case of SO_2 , the higher energy feature shown in Fig. 13 actually makes a larger contribution to the rates given in Fig. 19 than the lower energy feature.

Information about the dissociative-attachment rates for the species considered is needed not only for modeling of discharge processes in SF_6 but also for assessing the possibilities for detecting these species with analytical techniques which employ electron capture. The rate coefficients may also be needed to interpret data from mass spectrometric monitoring of ions in SF_6 glow discharges.

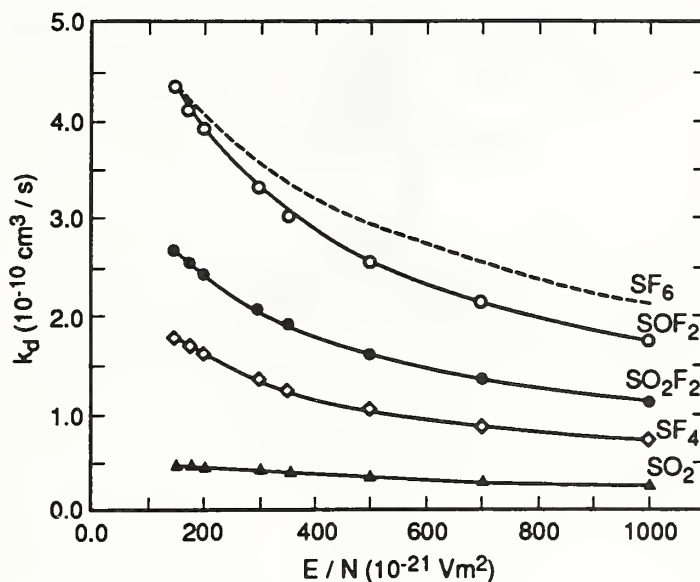


Figure 19. Calculated total dissociative electron attachment rate coefficients for SOF_2 , SO_2F_2 , SF_4 , and SO_2 in SF_6 as a function of E/N . The results for SF_6 are the same as given in Ref. 53.

2.3.5 Conclusions

SF_6 and the by-products of discharges in SF_6 exhibit total electron scattering cross sections whose magnitudes are comparable for all but threshold-energy electrons. By contrast, the magnitudes of the dissociative-attachment cross sections for these compounds vary over several orders of magnitude; several of the by-products have dissociative-attachment cross sections comparable in magnitude to the attachment and dissociative-attachment cross sections of SF_6 itself. It can thus be expected that the by-products in an SF_6 plasma are a significant source of negative ions and reactive radicals.

Temperature has a significant effect on the dissociative-attachment cross sections of SF_6 [66], SO_2 [50], and SO_2F_2 [59]. Plasma temperatures are often well above room temperature, and this temperature dependence of the cross sections presented here must be measured. This will be the focus of future work.

3 PARTIAL DISCHARGE AND DIELECTRIC LIQUID RESEARCH

Task 03

Kenneth L. Stricklett and Richard J. Van Brunt
Electricity Division
National Institute of Standards and Technology

3.1 Liquid Dielectrics

3.1.1 *Introduction*

Several fluids that are currently used or have potential for application in composite insulation systems were examined. Measurements include impulse breakdown voltage and high-speed photography of pre- and postbreakdown phenomena. The criteria for evaluating the performance of insulating materials are complex: The suitability of a fluid for a particular application may include such diverse characteristics as: chemical and thermal stability, flammability, loss tangent, dielectric constant, heat transfer, and electromagnetic compatibility to name a few. Hence, no single test can adequately qualify a material for use in an insulating system, and the results reported here are not intended for that purpose. The tests described below were undertaken primarily to allow critical examination of the methods used in this laboratory for measurement of breakdown voltages. Nevertheless, these results may prove useful in interpreting breakdown test results and provide additional experimental data on these materials.

3.1.2 *Breakdown Test Method*

A 5 mm test gap was formed by a steel gramophone needle having a tip radius of approximately 40 μm and a hemispheric stainless steel electrode having a 1.2 cm radius of curvature. For the majority of the results reported here, the electrodes were mounted within a test cell that was constructed from dielectric plastics; the cell is shown schematically in Fig. 20. Tests were also performed using a metallic test cell and are discussed separately below. The test cell was fitted with windows on two faces to permit photography of the gap, and the region between the electrodes was illuminated by a xenon flash lamp for this purpose. A negative-going voltage impulse, derived from a pulse transformer and a pulse-forming network, was applied to the gap. Polarity effects were investigated by reversing the electrical leads to the cell. Simultaneous records of the voltage waveform and of prebreakdown streamer growth

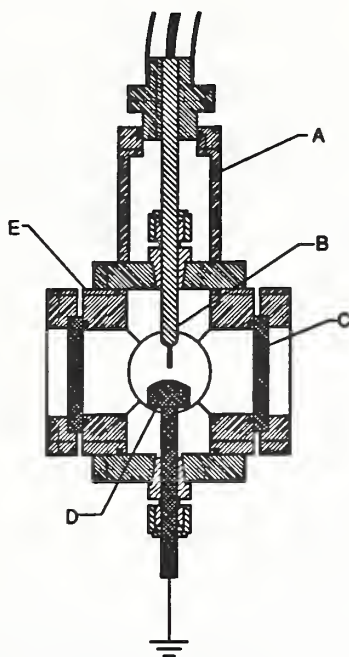


Figure 20. Schematic of the test cell used for breakdown studies in dielectric fluids. The high-voltage feed-through A, needle electrode, B, window, C, spherical electrode, D and test cell body, E, are indicated.

were obtained using a precision resistive divider and an image-converter camera. The voltage waveform and camera timing information were recorded digitally and stored for analysis [69]. The crest voltage, V_{cr} , breakdown voltage, V_{bd} , and the time-to-breakdown, t_{bd} , may be obtained directly from the recorded waveform, as illustrated in Fig. 21.

The initiation and growth of streamers were recorded photographically using shadowgraphic techniques. Low- and high-magnification photographs were obtained at rates ranging from 2×10^6 to 2×10^7 frames/s. Overall streamer velocities were determined from the low-magnification photographs using the change in position of the streamer tip between successive frames. A similar procedure, when applied to post-breakdown shockwaves, produced a mean value for the velocity of sound. The high-magnification pictures were used to determine the initial streamer velocity and the inception voltage, V_{inc} . Estimates of V_{inc} were obtained by averaging the voltages corresponding to the first frame showing the onset of streamer growth and the preceding frame [68].

Earlier studies have shown that pressure influences both the structure of prebreakdown streamers and the breakdown voltage of dielectric fluids [68, 70], with, in general, the dielectric strength increasing with pressure. Pressure effects were examined for one material, a perfluorinated polyether (PFPE). There is a clear correlation between cavitation in the fluid and the onset of electrical discharge activity

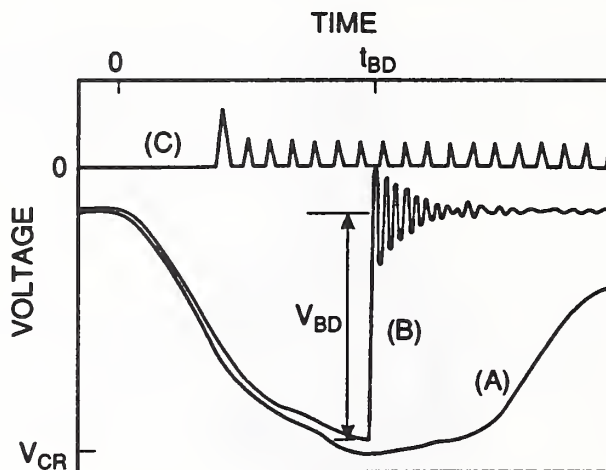


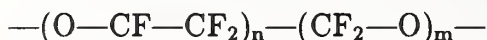
Figure 21. Voltage pulse and camera monitor traces: Voltage waveform (A) with breakdown (B), camera monitor pulses (C).

correlation between cavitation in the fluid and the onset of electrical discharge activity in hydrocarbon-based fluids. Two explanations have been offered to account for this observation: localized heating and vaporization of the fluid by electron and ion bombardment; or, alternatively, free charge in the fluid could result in an instability at the interface between the fluid and the electrode. In either case, the ambient pressure would influence the onset for cavitation. In selecting PFPE for this study, its high boiling point, as compared to hydrocarbons, and low vapor pressure may influence the mechanism for discharge initiation.

To achieve pressures above atmospheric, compressed nitrogen was admitted to a small cylinder connected to the test cell: the cylinder was partially filled with the fluid and the volume above the liquid was filled with compressed gas. Similarly, to study the fluid's behavior at reduced pressures, a mechanical vacuum pump, operating through a liquid-nitrogen trap, was used to evacuate the gas volume above the fluid. For the latter case, the liquid had to be degassed for about 12 hours before testing could begin due to outgassing from the fluid. Under either condition the test fluid was not circulated during electrical tests.

3.1.3 Perfluorinated Polyether

Because of their desirable chemical and physical properties, perfluorinated hydrocarbons have been applied in the electric and electronic industries. These fluids are more dense than conventional, hydrocarbon based insulating fluids, thus making them good heat transfer media. Additionally, they are relatively inert and non-flammable. Recently, a new family of PFPE's having the general formula



PROPERTY	UNITS	TEMPERATURE (°C)	VALUE
Viscosity	cm ² /s	20	52
Density	g/cm ³	20	1.85
Surface tension	dyne/cm	20	20
Volatility	% wgt. loss	120 (22h)	< 9
Pour Point	°C		-42
Flash Point	°C		none
Spec. heat	cal/g °C	38	0.24

Table 1. Physical properties of Galden HT-40.

|
CF₃

has become commercially available. These are colorless and odorless liquids that are, according to the manufacturer's specifications, non-flammable and non-toxic. The physical properties of the fluid depend on its composition, and may thus be tailored to meet specific requirements; the viscosity, for example, ranges from 0.8 to 60×10^{-2} cm²/s at 20° C, depending on the average molecular weight. They are typically more dense than perfluorinated hydrocarbons. In view of these physical and chemical properties PFPE's may also be of value in composite electrical insulation. In addition to their commercial potential, since PFPE's are fluorine bearing, they are likely electrophilic. This property may influence the initiation of the discharge and subsequent gas phase electrical discharge [67]. Since these perfluoro polyethers represent potentially interesting electric insulating fluids, their behavior under electrical impulse conditions was investigated. Preliminary results of these tests are reported here.

A representative PFPE having an average molecular weight of 4000 unified atomic mass units was selected for this study: The fluid tested is distributed under the Galden HT-40 trade name. For the convenience of the reader, several of the manufacturer's data are shown in Table 1. The fluid was used as received, without further purification other than that which occurred during testing by filtration through a 2- μ m-pore-sized paper filter.

3.1.4 Results

Results obtained for the negative point (point cathode) and for the positive point (point anode) are summarized in Table 2. As shown, the breakdown voltage and streamer velocity depend on polarity. The breakdown voltage, is nearly independent of polarity; this characteristic apparently differs from simple hydrocarbons and petroleum-derived insulating oils where the magnitude of the breakdown negative

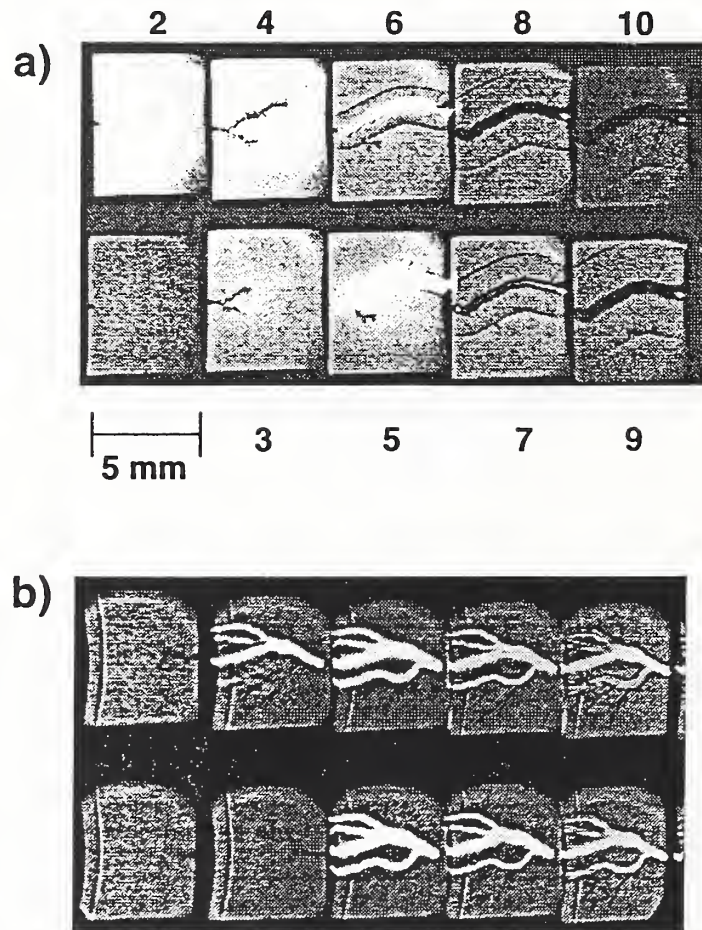


Figure 22. Negative and positive streamers in PFPE. “Point plane” test gap with 5 mm electrode spacing. The crest voltage is approximately 49 kV: (a) negative needle at 200 ns between frames; (b) positive needle at 50 ns between frames. The frame sequence is shown in (a).

voltage for a negative point is typically greater than that for a positive point. Representative photographic data obtained at low magnification are shown in Fig. 22. Note that positive streamers move about ten times faster than negative and that the frame rates for the two photographs differ accordingly.

A post-breakdown shockwave created by the arc may be clearly seen in the latter frames of Fig. 22a. Assuming the shock is weak, the rate of propagation of the wave should be constant and approximately equal to the sonic velocity [76]. Measurement of the diameter of the shock yielded an estimate of the sonic velocity for PFPE of $8.0 \pm 0.2 \times 10^4$ cm/s.

High magnification photographs of streamer initiation at the electrode surface are shown in Fig. 23 for both polarities. Close examination of these pictures reveals that cathode streamers initially propagate at speeds on the order of $1 \pm 0.5 \times 10^4$ cm/s,

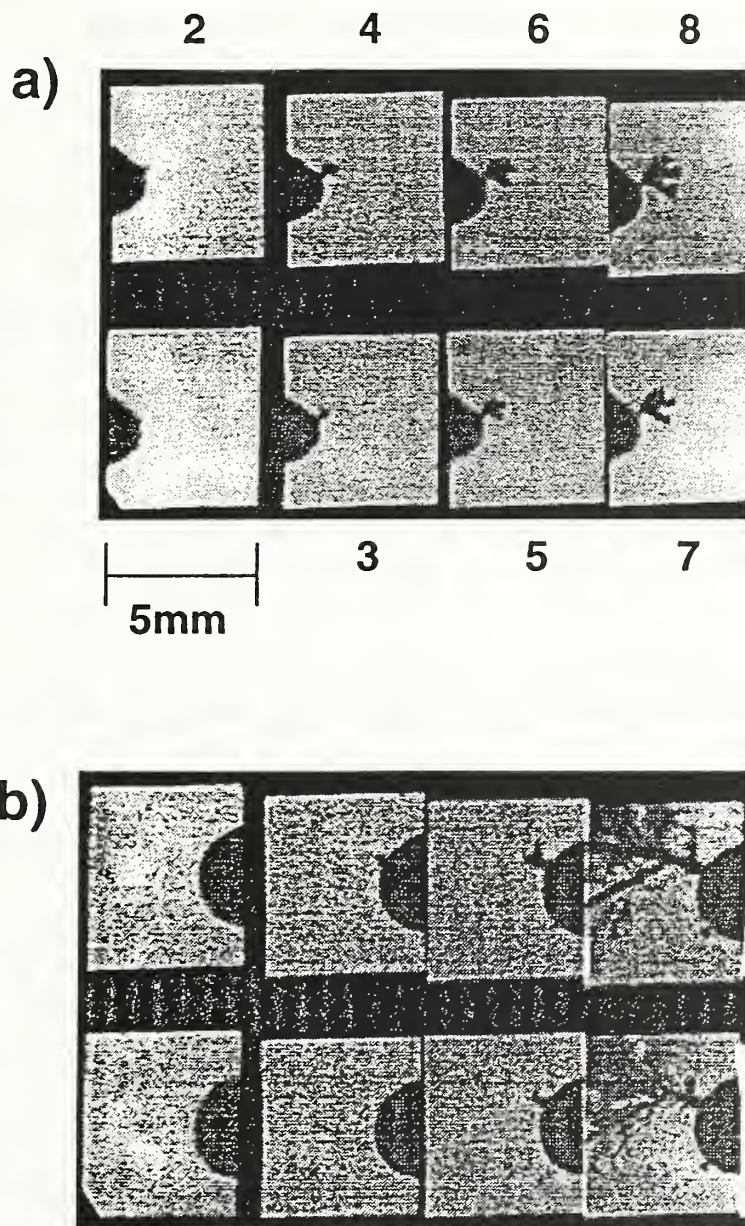


Figure 23. High-magnification photographs of streamer initiation

	Needle Cathode	Needle Anode
Crest Voltage (kV)	49	49
Breakdown Voltage (kV)	40 ± 1	42 ± 2
Time to breakdown (μs)	3.8 ± 0.2	3.9 ± 0.5
# Breakdowns/# Pulses	32/32	8/8
Streamer speed ($\times 10^5$ cm/s)	4.5 ± 0.5	30 ± 0.4

Table 2. Effect of polarity on electrical breakdown in PFPE. "Point plane" electrode geometry, 5 mm gap; atmospheric pressure.

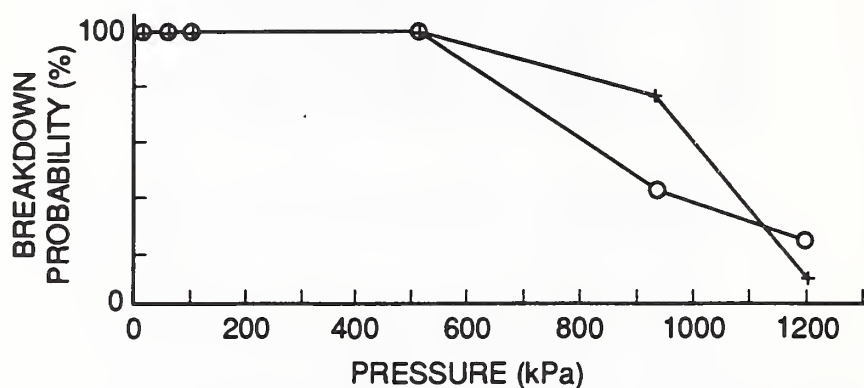


Figure 24. Pressure dependence of breakdown probability for PFPE.

approximately one tenth the sonic velocity. The rate of propagation at their initiation differs substantially from the average speed crossing the gap, as may be verified by examination of the low-magnification photographs and comparison with the average speed given in Table 2. The negative streamer grew to 10 to 15 μm , on average, after which the growth rate increases considerably. Similar behavior has been noted for negative streamers in simple hydrocarbons [71]. The photograph for the positive point also shows evidence of a slow, subsonic, growth phase. However, due to the high variability of the streamer inception time and voltage, and the short time interval between inception and breakdown, systematic investigation of the initiation of the positive streamer requires a different experimental approach as discussed below.

The effect of pressure on streamer inception is summarized in Table 3. All quantities measured, V_{inc} , V_{bd} and T_{bd} for both polarities appear to have positive correlation with pressure. It should be noted that the breakdown voltages and times-to-breakdown listed in Table 3 do not fully represent the effect of pressure: At the highest pressure tested, the gap did not breakdown for a significant fraction of pulses and thus did not contribute to the mean values reported. To further emphasize this point, the breakdown probabilities for both polarities are plotted as a function of pressure in Fig. 24, and clearly show pressure to have a pronounced influence on dielectric strength for both polarities.

Press. (kPa)	Pulses	V_{inc} (kV)	V_{bd} (kV)	t_{bd} (μ s)
Needle cathode				
3	7	30 \pm 3 (7)	39 \pm 1 (7)	4.1 \pm 0.2 (7)
50	7	29 \pm 3 (7)	39 \pm 1 (7)	4.3 \pm 0.3 (7)
100	7	29 \pm 2 (7)	39 \pm 1 (7)	4.3 \pm 0.3 (7)
510	7	33 \pm 2 (7)	40 \pm 1 (7)	4.5 \pm 0.3 (7)
930	7	33 \pm 3 (6)	41 \pm 1 (3)	5.8 \pm 0.3 (3)
1100	7	36 \pm 3 (5)	42 \pm 1 (2)	5.1 \pm 0.2 (2)
Needle anode				
12	9	53 \pm 1 (4)	53 \pm 1 (9)	2.6 \pm 1 (9)
57	8	53 \pm 1 (5)	54 \pm 2 (8)	3.1 \pm 0.3 (8)
100	37	54 \pm 3 (12)	55 \pm 3 (37)	3.2 \pm 0.4 (36)
510	23	51 (1)	58 \pm 5 (23)	3.8 \pm 0.7 (23)
930	9	—	64 \pm 1 (7)	5.0 \pm 0.5 (7)
1200	9	62 (1)	61 (1)	4.2 (1)

Table 3. Effect of pressure on streamer inception, breakdown voltage, and time-to-breakdown in PFPE. Mean values of inception voltage, V_{inc} , breakdown voltage, V_{bd} , and time-to-breakdown, t_{bd} , are given. The sample size is shown in parentheses to the right of each value. The stated uncertainty is one standard deviation. A nominal 42 kV crest voltage was used for the needle cathode tests while that for the needle anode was 65 kV.

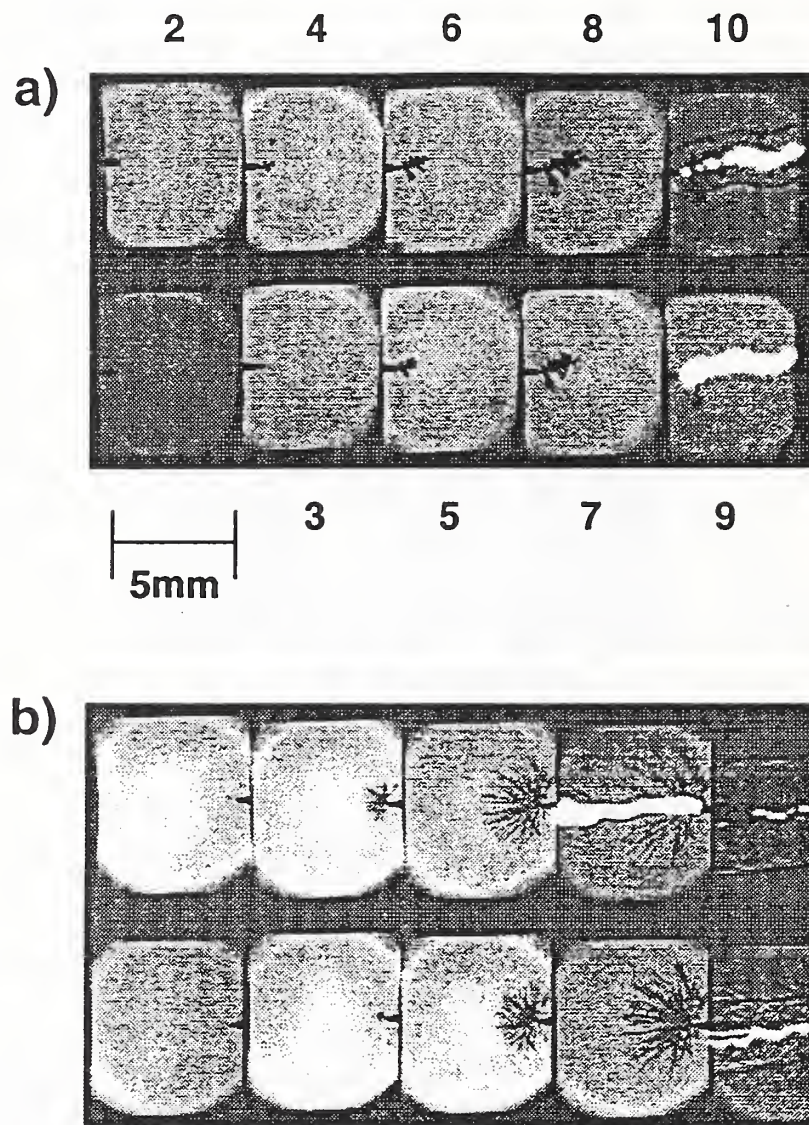


Figure 25. Representative photographic data for DTE.

Pressure (kPa)	incidence	length (max)	persistence (ns)
100	$50 \pm 8\%$ (19/38)	40 μm	100
15	$73 \pm 7\%$ (27/37)	40 μm	100

Table 4. Statistical data for subsonic positive streamers in PFPE. “Point-plane” electrode geometry, 3 mm gap.

3.1.5 *Positive Streamer Initiation in PFPE*

The pressure dependence noted in the dielectric strength for the positive point motivated further tests. The pressure dependence observed for hydrocarbon-based fluids for the negative point has been attributed to cavitation that occurs at the initiation of the streamer. Increased pressure is thought to delay the onset, and in general, to suppress cavitation. The subsonic phase of streamer growth has been associated with the deformation of the cavity under the influence of the electrical field and, for the negative point, is well documented. Under a very limited range of experimental conditions, subsonic positive streamers have also been reported [77]. The generation of a gas-phase volume at the initiation of the positive streamer would provide qualitative interpretation of the observed pressure dependence, and photographic methods may be used to test for the presence of a slow-growing streamer. However, previous observations of this phenomena have been limited to experimental conditions near the threshold for streamer initiation due to the high rate of propagation of positive streamers.

The inclusion of an optical delay in the light path between the test cell and the camera, however, allows a different experimental approach. Provided the effective optical delay, that is, the time-of-flight minus the camera trigger delay, is greater than the time delay between streamer initiation and breakdown, the camera may be triggered by the breakdown current rather than by an externally generated trigger. A similar technique has been used in this laboratory to investigate the relative probabilities of breakdown via negative and positive streamers in a uniform field [78].

The results of these tests are summarized in Table 4 and show a high incidence for the appearance of a microscopic object at the streamer initiation site. Although this structure was not visible in all of the photographs, this can be easily accounted for by the size of the structure at its maximum extent and the distribution of initiation sites on the needle tip. The incidence rate for the appearance of the structure increases upon lowering the ambient pressure, and the apparent rate growth for the structure is on the order of 10^4 cm/s. All of these observations are consistent with cavitation at the electrode surface at the streamer initiation site and suggest that the onset of cavitation plays a principal role in the initiation of positive streamers in this material.

	Needle Cathode	Needle Anode
Crest Voltage (kV)	120	54
Breakdown Voltage (kV)	114 ± 7 (7)	52 ± 5 (24)
Time to breakdown (μ s)	4.6 ± 0.7 (7)	5.7 ± 0.8 (24)
# Breakdowns/# Pulses	7/7	24/31
Streamer speed ($\times 10^5$ cm/s)	0.20 ± 0.09	$1.2 \pm .5$

Table 5. Effect of polarity on electrical breakdown ditolyl ether. Gap: 5 mm, atmospheric pressure.

	Needle Cathode	Needle Anode
Crest Voltage (kV)	89	60
Breakdown Voltage (kV)	87 ± 1 (4)	58 ± 1 (7)
Time to breakdown (μ s)	5.6 ± 0.5 (4)	5.2 ± 0.7 (7)
# Breakdowns/# Pulses	4/5	7/7
Streamer speed ($\times 10^5$ cm/s)	1.1 ± 0.3	$1.2 \pm .3$

Table 6. Effect of polarity on electrical breakdown benzyl and dibenzyl toluene. "Point-plane" electrode geometry with 5 mm inter-electrode spacing, atmospheric pressure.

3.1.6 Ditolyl Ether

Results of impulse breakdown tests for ditolyl ether (DTE) are summarized in Table 5, and representative photographic data are shown in Fig. 25. The sonic velocity is estimated to be $1.8 \pm 0.1 \times 10^5$ cm/s in this material.

3.1.7 Benzyl and Dibenzyl Toluene

Electrical breakdown tests were also performed on a commercially available mixture of benzyl and dibenzyl toluene, the material is distributed under the C101 trade name. Representative photographs of prebreakdown streamer growth are shown in Fig. 26, and breakdown measurements obtained for both polarities are summarized in Table 6. The sonic velocity is estimated from the rate of the propagation of the shock created by breakdown and is $1.8 \pm 0.1 \times 10^5$ cm/s.

3.1.8 Discussion and Conclusions

The method for impulse testing described above required physically breaking and remaking electrical connections to the test cell to change polarity. This practice may introduce unwanted variability and a systematic error in the measured breakdown voltage. In all cases the prebreakdown streamer initiated at the needle tip, the

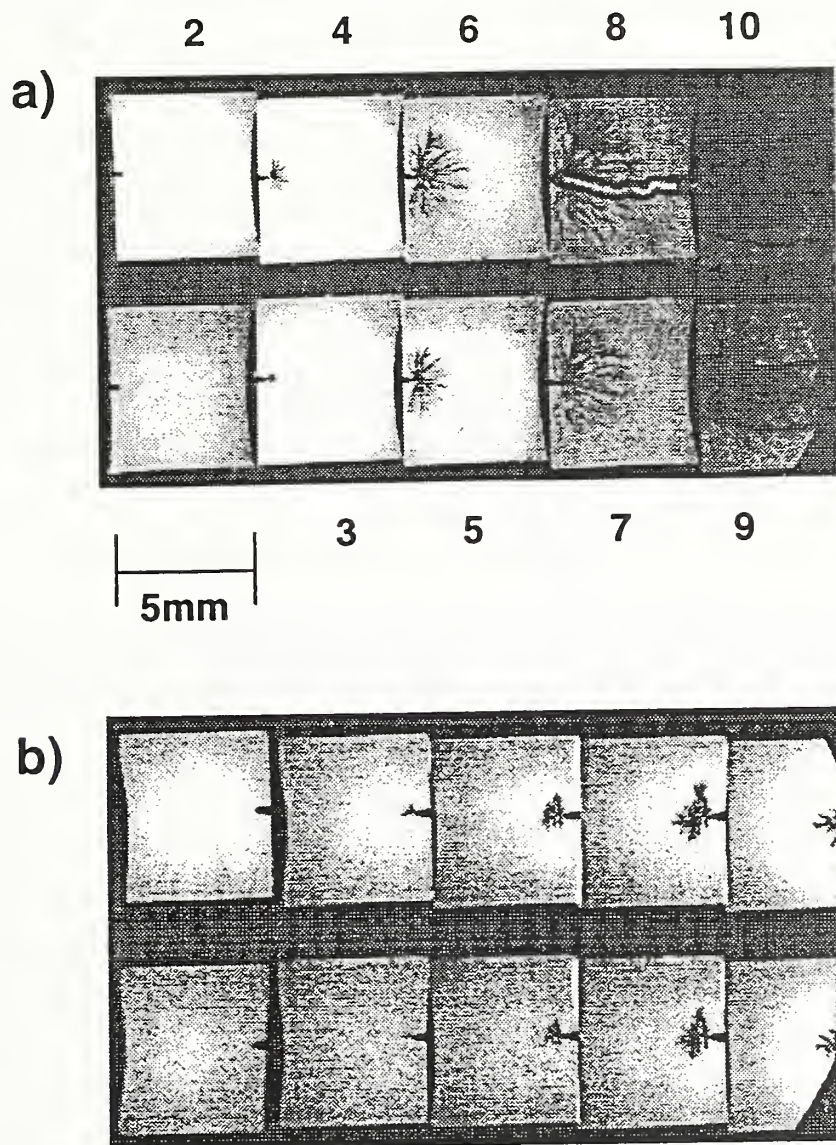


Figure 26. Representative photographic data for a mixture of benzyl and dibenzyl toluene. The point cathode and point anode polarities are shown in a) and b) respectively. The data were obtained at atmospheric pressure. The interval between frames for the point anode is nominally 500 ns while that for the point cathode is 200 ns.

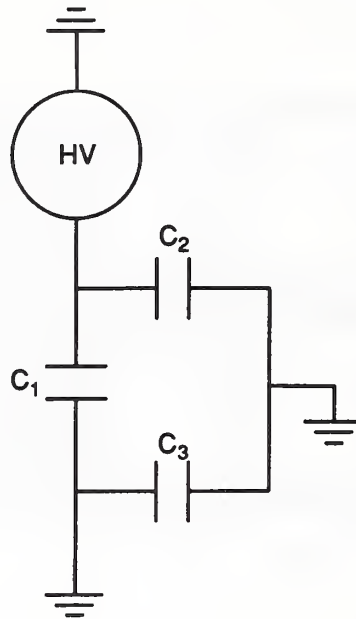


Figure 27. Test cell equivalent circuit. C_1 , is the capacitance between the electrodes; C_2 and C_3 are, respectively, the capacitance of the needle electrode and low curvature electrode to ground.

region of highest electrical stress, and it thus seems reasonable to conclude that the breakdown voltage depends critically on the strength of the electric field in that region. Thus any change of electrode geometry that influences the magnitude of the electric field at the needle tip will introduce an error. The test cell may be modelled by the circuit shown schematically in Fig. 27, where C_1 is the capacitance between the needle and the low curvature electrode, and C_2 and C_3 are the capacitance of the needle and low curvature electrodes to ground, respectively. In general C_3 is greater than C_2 and their relative magnitude influences the strength of the electric field at the needle tip. Neglecting space charge, the electric field at the needle tip is strictly a function of the applied voltage and the gap geometry and, for the circuit shown in the figure, it is proportional to $C_1 + C_2$. Upon reversing the electrical leads, the field strength is proportional to $C_1 + C_3$. Hence for the same applied voltage, the ratio of the positive point field to the negative point field is given by

$$\frac{E_+}{E_-} = \frac{C_1 + C_2}{C_1 + C_3}. \quad (17)$$

Measurement of the applied voltage alone is, therefore, not sufficient to characterize the system, and the difference between C_2 and C_3 tends to bias the measured positive point breakdown voltage to lower values. To test for this possibility, capacitance measurements were made on a metallic test cell. Since the electrodes are in close proximity to a grounded metallic cell this is, in a sense, a worst case test. Measurements of C_1 , $C_1 + C_2$ and $C_1 + C_3$ for the metallic cell yielded 3.5, 4.4 and

6.0 pF respectively. These values suggest that the electric field at the needle may be significantly modified by stray capacitance.

Although the pulse generator used for these measurements yields a highly reproducible pulse, the shape of the voltage waveform requires that results of these tests be carefully interpreted. Electrical breakdown is known to depend both on the level of stress and the time of exposure to stress. Thus measurement of the breakdown voltage alone may not be an adequate measure of the dielectric strength of the material. Careful examination of the data shown in Table 3, for example, reveals that although the breakdown voltage appears to have a slight dependence on pressure, both the inception voltage and the time-to-breakdown are clearly correlated with the ambient pressure. This apparent contradiction may be reconciled by noting that the time-to-breakdown at the highest pressure tested lies near the peak of the voltage waveform, where the voltage is relatively constant, and that the gap is stressed for a relatively long time. Any conclusion drawn from the breakdown voltage alone would thus misrepresent the effect of pressure on the electrical behavior of this material.

For several of the results presented above, the gap broke down at times after the crest voltage and thus yields an ambiguous breakdown voltage. This characteristic of the impulse waveform may be overcome by increasing the stress on the material, that is, by forcing breakdown to occur on the leading edge of the impulse. However, photographic studies under these conditions are of limited value since the temporal development of the prebreakdown streamer is typically limited to only one or two frames.

The fluids tested differ most notably in their rates of streamer propagation: streamers in both DTE and C101 propagate at subsonic velocities for a significant fraction of the gap, while streamers of both polarities in PFPE appear to go over to supersonic propagation rates very early in their growth. This difference must be properly accounted for in comparing test results for these materials. In particular, if the applied voltage changes appreciably in the time required for the streamer to cross the gap, the voltage at the time of breakdown may be poorly correlated to the dielectric strength of the material.

In conclusion, the methods described above appear to be best suited to studies that include the variation of a single experimental parameter, as is the case for the pressure dependence observed in PFPE. Comparison of test results for different materials requires careful evaluation of several confounding issues, such as the time variation of the applied voltage and streamer propagation rates. The interpretation of comparative test results may be simplified by prudent choice of voltage waveform. For example, a voltage ramp or step may be preferable to the voltage waveform used for these tests. Finally, the accuracy of the test would be improved by providing a bipolar impulse voltage so that capacitive effects may be reduced.

3.2 Partial Discharge Measurements

3.2.1 Introduction

There has been considerable recent interest in the use of data on the phase-resolved stochastic properties of partial discharges (PD's) to extract information about the characteristics of point defects and electrically-induced aging of solid insulating materials [79–88]. Phase-resolved PD pulse-height and phase-of-occurrence distributions typically exhibit complex structures that are not easily interpreted and may be difficult to reproduce. The relationship between the observed PD-pulse distributions and the physical mechanisms that determine the stochastic behavior of PD's have never been carefully analyzed or clearly elucidated.

It is shown in the present work using a point-dielectric discharge gap that the phase-resolved stochastic behavior of ac-generated PD's is strongly influenced by phase-to-phase memory propagation, where the "memory" is associated with charging of dielectric surfaces by successive discharge events. The memory effects are revealed for the first time from measurements of phase-restricted *conditional* partial-discharge amplitude and phase-of-occurrence distributions that show, for example, that the most probable phase-of-occurrence of a PD pulse on one half-cycle of the applied voltage is dependent on the total charge deposited by PD's on the dielectric surface during the previous half-cycle. The effects of memory uncovered are implied by previous descriptions of the PD phenomenon when account is taken of statistical variability in the charging of the dielectric surface.

The specific purposes of the present work are: 1) to show how memory propagation complicates the interpretation of phase-resolved pulse-height or phase-of-occurrence distributions and causes such distributions to become susceptible to nonstationary behavior; 2) to show how memory effects can be unraveled by measuring or computing various *conditional* pulse-amplitude and phase distributions; and 3) to introduce a method for real-time measurement of conditional distributions.

3.2.2 Significance of Memory Propagation

It can be argued that, in general, pulsating PD phenomena are complex non-Markovian stochastic processes in which memory effects play an important role [86,87]. Memory effects arise because of the influence of residuals from previous discharge pulses, e.g., surface charge, ion space charge, and species in metastable excited states, on the initiation and development of subsequent discharge pulses. The existence of memory implies that the amplitude and phase of any discharge pulse can depend on the amplitudes and phases-of-occurrence of pulses that occurred at earlier times. Two consequences of memory propagation are: 1) the interpretation of measured PD-pulse amplitude and phase distributions becomes nontrivial, and 2) the

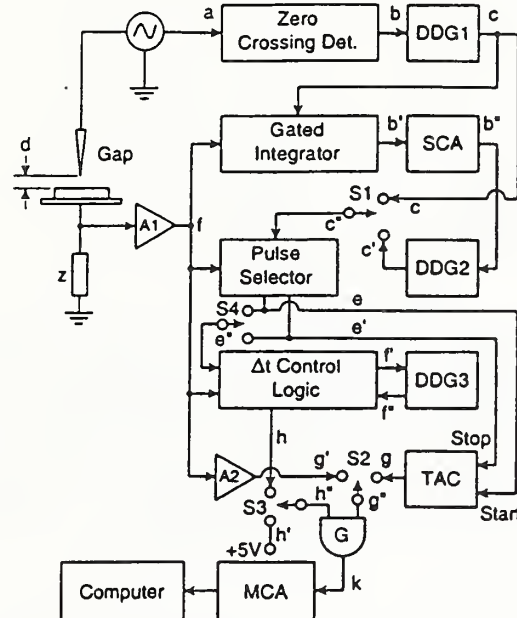


Figure 28. Stochastic analyzer. The individual components are defined as follows: A-amplifier, G-gate, S-switch, DDG-digital delay pulse generator, MCA-multichannel analyzer, SCA-single channel analyzer, TAC- time-to-amplitude converter. The Δt control logic circuit is similar to that previously described [90].

phenomena tends to exhibit nonstationary behavior. Nonstationary behavior results in an inability to obtain reproducible data for measured statistical distributions even from “controlled” experiments in which PD’s are generated in simple, well defined discharge gaps under ostensibly identical conditions. Because of non-stationary behavior, PD amplitude and phase distributions can exhibit random, unpredictable changes with time. Such unpredictable changes can arise, for example, because of the correlation between PD pulse amplitude and the time that has elapsed since the last PD event. If pulse amplitude and time separation are not independent random variables, then any effect that changes the time distribution between pulses will also change the amplitude distribution.

3.2.3 Real-Time Stochastic Analyzer

Figure 28 shows a block diagram of a stochastic analyzer that is used to measure, in real time, a set of conditional and unconditional pulse-amplitude and phase-of-occurrence distributions. It is an extended version of a previously described device [87, 89] that was used to obtain data on the stochastic properties of dc corona pulses.

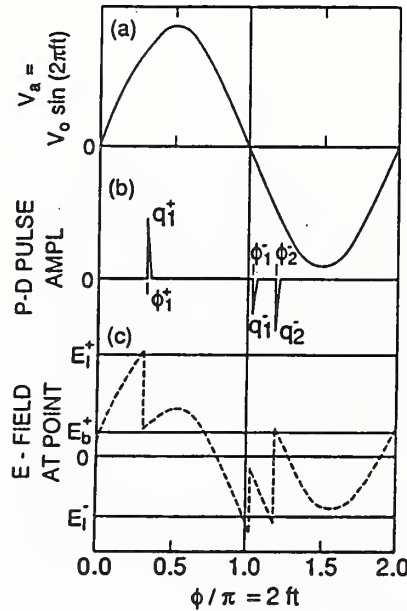


Figure 29. Diagrammatic representation of an ac-excited PD process: a) applied ac voltage; b) PD pulse amplitudes q_i^\pm and phase-of-occurrence ϕ_i^\pm ; c) phase dependence of the spatially averaged electric-field strength near the point electrode.

In addition to the distributions previously measured, the present version allows measurement of many different phase-restricted distributions needed to characterize the stochastic behavior of ac-generated PD's.

Table 5 shows a partial list of the additional phase-restricted distributions that can be measured with this system. The notation used in this table can be understood from consideration of the diagram in Fig. 29

The unconditional distributions, $p_o(q_i^\pm)$ and $p_o(\phi_i^\pm)$ are defined such that, for example, $p_o(q_1^-)dq_1^-$ is the probability that the first PD pulse on the negative half-cycle has an amplitude between q_1^- and $q_1^- + dq_1^-$ independent of previous discharge history. The half-cycle is defined in Table 5 to be shifted in phase by a small amount $\delta\phi$ to allow for the possibility that the first pulse will occur before the voltage zero crossing. The first order conditional distributions are defined such that, for example $p_1(\phi_2^- | Q^+)d\phi_2^-$ is the probability that the second PD pulse on the negative-half cycle occurs at a phase between ϕ_2^- and $\phi_2^- + d\phi_2^-$ if the sum of the PD charges on the preceding half-cycle has a value Q^+ . The value of Q^\pm is specified by the measurement procedure to lie within a range $(Q_{min}^\pm, Q_{max}^\pm)$. In the second-order conditional distribution $p_2(q_i^\pm | Q^\pm, \phi_i^\pm)$ both Q^\pm and ϕ_i^\pm lie within specific ranges. The conditional distributions $p_i(q_j^\pm | \Delta\phi_{u,l}^\pm)$ and $p_1(\phi_j^\pm | \Delta\phi_{u,l}^\pm)$ considered in earlier work [79-88] are phase-resolved amplitude and probability-of-occurrence distributions that contain no information about memory propagation.

Table 5

Conditional (p_1 and p_2) and unconditional (p_o) PD pulse amplitude and phase distributions considered in the present work.

Pulse-Amplitude distributions	Phase-of-occurrence distributions	Phase restrictions
$p_o(q_i^\pm)$	$p_o(\phi_i^\pm)$	$\phi_i^+ \in (-\delta\phi, \pi - \delta\phi)$ $\phi_i^- \in (\pi - \delta\phi, 2\pi - \delta\phi)$
$p_1(q_j^\pm \Delta\phi_{u,l}^\pm)$	$p_1(\phi_j^\pm \Delta\phi_{u,l}^\pm)$	$\Delta\phi_{u,l}^\pm = \phi_u^\pm - \phi_l^\pm$ $\phi_j^\pm \in (\phi_l^\pm, \phi_u^\pm)$
$p_1(q_i^\mp Q^\pm)$	$p_1(\phi_i^\mp Q^\pm)$	$Q^\pm = \sum_k q_k^\pm(\phi_k^\pm)$
$p_2(q_i^\pm Q^\mp, \phi_i^\pm)$		$\phi_k^+ \in (-\delta\phi, \pi - \delta\phi)$ $\phi_k^- \in (-\pi - \delta\phi, -\delta\phi)$ $i = 1, 2, 3, \dots$ $j \geq 1, k \geq 1$

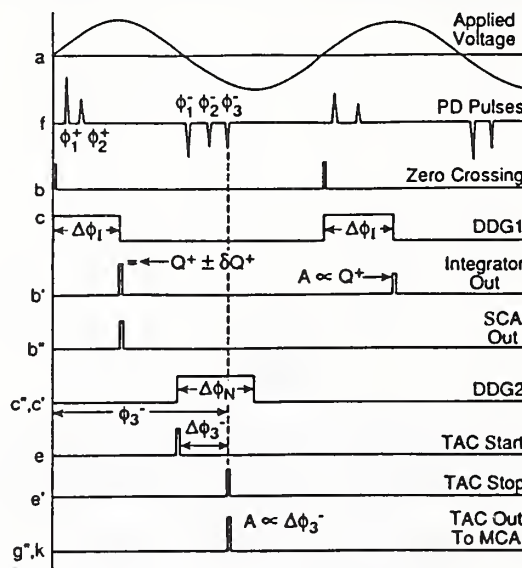


Figure 30. Pulse diagram corresponding to the different indicated circuit points in Fig. 28 for measurement of $p_1(\phi_3^- | Q^+)$.

The different components that comprise the measurement system shown in Fig. 28 are defined in the figure caption. A detailed explanation of how this system works cannot be covered in this brief report. A complete documentation of the system operation together with descriptions of the individual circuits is now in preparation.

Figs. 30 and 31 show pulse diagrams for the different circuit locations in Fig. 28 that apply respectively to the measurement of the conditional distributions $p_1(\phi_i^\pm | Q^\mp)$ and $p_2(q_i^\pm | \phi_i^\pm, Q^\mp)$ for which examples of data are shown in the next section.

The combinations of switch configurations (S1-S4 in Fig. 28) that are required to measure the distributions $p_o(\phi_i^\pm)$, $p_1(\phi_i^\pm | Q^\mp)$, and $p_2(q_i^\pm | \phi_i^\pm, Q^\mp)$ are shown in Table 6. It is also possible to configure the system in other ways to measure many other conditional distributions such as, for example, $p_2(\phi_i^- | q_{i-1}^-, \phi_{i-1}^-)$, $p_2(q_i^- | \phi_{i-1}^- - \phi_{i-1}^-)$, and $p_1(\phi_{ij}^- | Q_{j-k}^+)$, $j \geq k$. In the latter distribution, ϕ_{ij}^- is the phase-of occurrence of the i th pulse in the j th negative half-cycle and Q_{j-k}^+ is the net charge of all PD's on the $j - k$ th positive half-cycle. The conditional distributions indicated in Table 6 were selected for consideration here because they can be interpreted easily and unambiguously in terms of expected memory propagation from half-cycle to half-cycle.

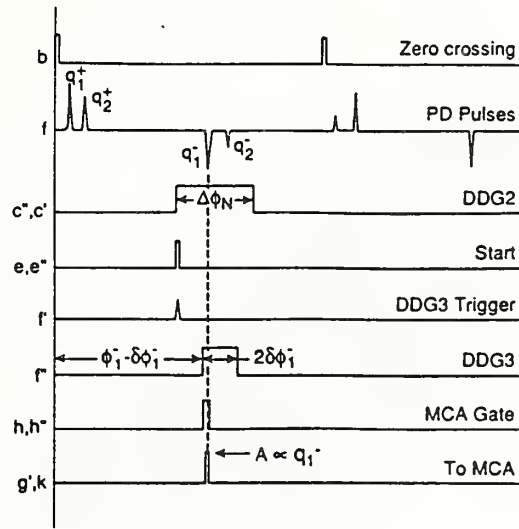


Figure 31. Pulse diagram for measurement of $p_2(q_1^- | Q^+, \phi_1^-)$.

Table 6 - Configuration of switches in Fig. 8 for measurement of the different indicated distributions

Switch	$p_o(\phi_i^\pm)$ $i = 1, 2, \dots$	$p_1(\phi_i^\pm Q^\mp)$ $i = 1, 2, \dots$	$p_2(q_1^\pm Q^\mp, \phi_1^\pm)$
S1	$c'' = c$	$c'' = c'$	$c'' = c'$
S2	$g'' = g$	$g'' = g$	$g'' = g'$
S3	$h'' = h'$	$h'' = h'$	$h'' = h$
S4	—	—	$e'' = e$

3.2.4 Experimental Arrangement

To test the measurement system described above, partial discharges were generated by applying an ac voltage across a point-to-dielectric electrode configuration in air similar to that used in a previous investigation [91]. A sharp (less than 0.05 mm radius) stainless-steel needle was positioned directly above the center of a circular polytetrafluoroethylene (PTFE) dielectric wafer attached to a metallic plane electrode. The PTFE thickness and diameter were, respectively, 1 mm and 3.0 cm. A sinusoidal voltage with an rms value of either 3.0 or 2.4 kV at either 120 or 200 Hz was applied to the electrodes. The point-to-electric gap spacing (d) could be adjusted between 0.0 and 10.0 cm. The results reported here were obtained under conditions where the discharge was reasonably stationary in its behavior. The discharge characteristics changed significantly as d was varied. For $d > 0$, the negative

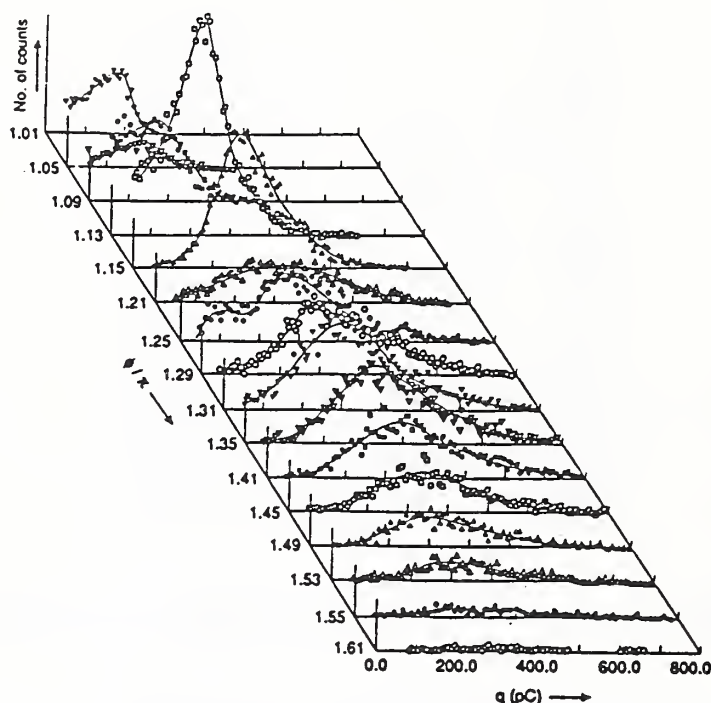


Figure 32. Phase-resolved PD pulse-height distributions for a point electrode on ($d = 0.0$ cm) a PTFE wafer of 3.0 cm diameter in air. The frequency is 200 Hz and the applied voltage is 2.5 kV rms. The results apply only to the negative half-cycle with a phase window per distribution of $\Delta\phi_{u,t} = 0.063$ radians.

PD pulses exhibit characteristics similar to those seen for dc-generated Trichel pulses [89]. At $d = 0$, the negative PD pulses appear to be fewer in number and more random than is the case for Trichel pulses.

3.2.5 Examples of Results

The partial discharges observed for the conditions considered here exhibited an asymmetric behavior with respect to the sign of the applied voltage consistent with the diagram in Fig. 29. On the average, for $d = 0$, one relatively large PD pulse occurred in the rising portion of the positive half-cycle and two or more smaller PD pulses appeared on the negative half-cycle. The asymmetry can be attributed in part to the presence of a preferred quasi-permanent positive charge on the PTFE surface as verified using electrostatic probe measurements. A constant positive charge density produces an effective dc bias in the average field, E , near the point electrode which is designated by E_b^+ in Fig. 29.

Shown in Fig. 32 are phase-resolved PD pulse-height distributions corresponding to

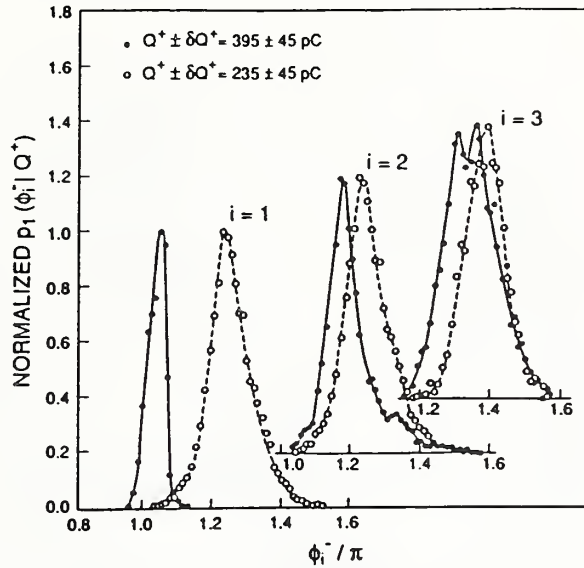


Figure 33. Measured conditional phase distributions of the first, second, and third PD pulses in the negative half-cycle for the two indicated ranges of values for the total charge associated with PD pulses during the previous half-cycle. The frequency is 200 Hz, applied voltage is 2.4 kV rms, and gap spacing is 0.0 cm.

$p_1(q_j^- | \Delta\phi_{u,l}^-), j \geq 1$, that apply to the negative half-cycle. The distributions exhibit a rapid phase dependence and a complexity of structure that is consistent with other observations [83–86]. The details of the phase dependencies and structures observed from the measurements of $p_1(q_j^- | \Delta\phi_{u,l}^-)$ are sensitive to the discharge gap conditions and consequently difficult to reproduce.

As will be discussed later, interpretation of data as shown in Fig. 32 is difficult because of phase-to-phase memory propagation revealed from measurements of $p_1(\phi_i^\pm | Q^\mp)$, $p_1(q_i^\pm | Q^\mp)$, and $p_2(q_i^\pm | Q^\mp, \phi_i^\pm)$ shown in Figs. 33–35.

The data on $p_1(\phi_i^- | Q^+)$ in Fig. 33 indicate that the most probable phase-of-occurrence of the i th pulse on the negative half-cycle depends significantly on the amount of charge, Q^+ , deposited by PD's during the previous half-cycle. The dependence of ϕ_i^- on Q^+ is great for the first pulse ($i = 1$) and at least for the third pulse ($i = 3$) as expected since charge deposited by each successive pulse in the same half-cycle tends to diminish memory of charges deposited during previous half-cycles.

The observed dependencies of ϕ_i^- on Q^+ are consistent with $E - \phi$ diagram as shown in Fig. 29 where E is the instantaneous average electric-field strength near the point electrode. It is assumed that a PD can initiate when the magnitude of E is greater than the onset values $|E_I^-|$ or $|E_I^+|$. The larger the amount of charge deposited on the dielectric during the preceding half-cycle, the greater will be the value of $|E|$ at a given phase on the next half-cycle, and hence, the greater will be the probability of

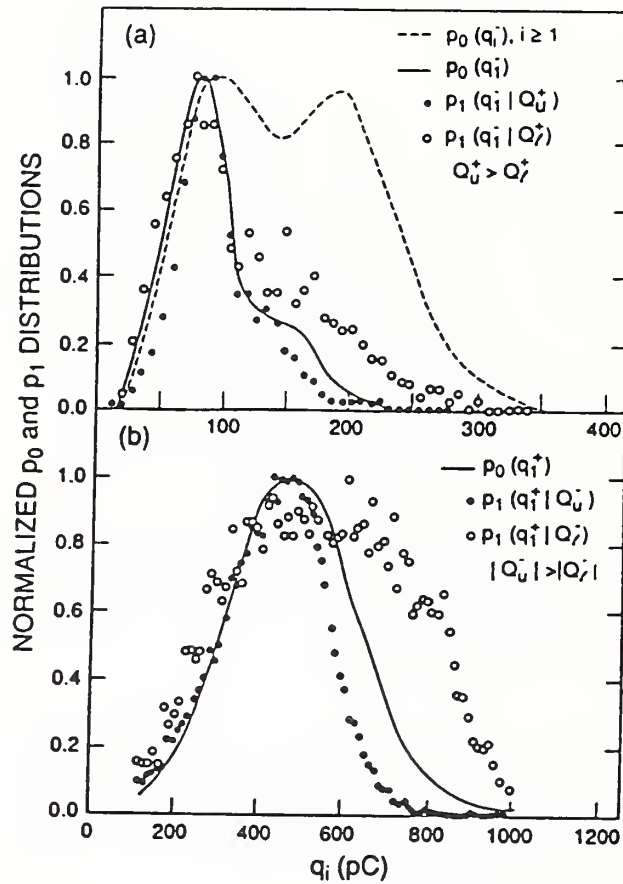


Figure 34. Measured conditional and unconditional PD pulse-amplitude distributions: a) for PD's on the negative half-cycle conditional on the amount of charge deposited in the previous positive half-cycle, where $Q_u^+ > 11$ pC and $Q_i^+ = 495 \pm 50$ pC; b) for PD's on the positive half-cycle conditional on the amount of charge deposited on the previous negative half-cycle, where $|Q_u^-| > 580$ pC and $|Q_i^-| = 205 \pm 25$ pC. The frequency is 120 Hz, applied voltage is 2.4 kV rms, and gap spacing is 0.0 cm.

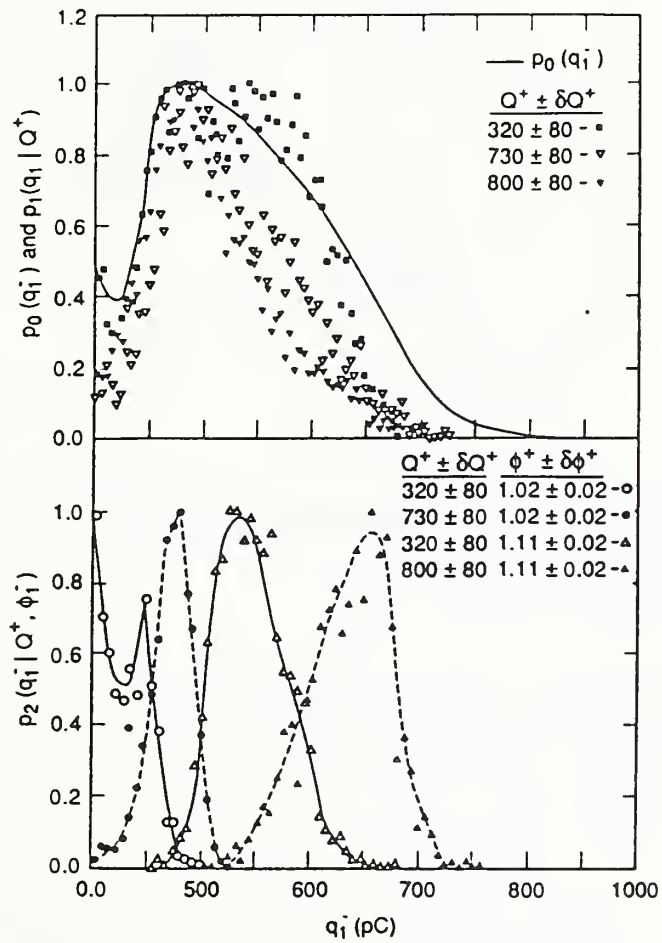


Figure 35. Measured unconditional and conditional PD pulse-amplitude distributions obtained using experimental conditions similar to those that apply to the data shown in Figs. 33 and 34.

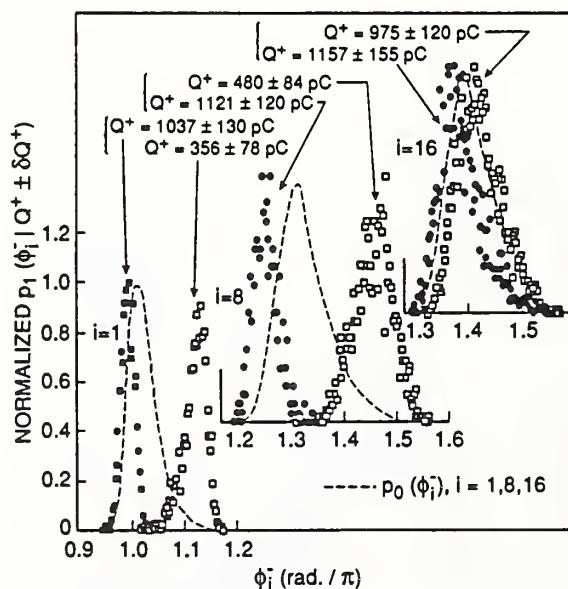


Figure 36. Measured conditional and unconditional phase-of-occurrence distributions for the 1st, 8th, and 16th pulses in the negative half-cycle. The frequency is 200 Hz, applied voltage is 3.0 kV rms and gap spacing is 1.5 mm.

PD initiation. It can therefore be expected, as observed, that when Q^+ is increased, the distribution in ϕ_i^- becomes peaked at a lower phase value.

The data on $p_1(q_1^\pm | Q^\mp)$ shown in Fig. 34 indicate that the PD pulse amplitudes also depend on charge deposited during the previous half-cycle. It is seen that the larger the value of $|Q^\mp|$, the smaller will be the mean value of q_1^\pm . The dependencies of $p_1(q_1^\pm | Q^\mp)$ on $|Q^\mp|$ are not easily interpreted from $E - \phi$ diagrams because of the strong dependence of q_1^\pm on ϕ_1^\pm . The corresponding conditional distributions $p_1(\phi_i^\pm | Q^\mp)$ and $p_1(q_i^\pm | Q^\mp)$ are related from the law of probabilities by the integral expression

$$p_1(q_i^\pm | Q^\mp) = \int_{\phi_{min}}^{\phi_{max}} p_1(\phi_i^\pm | Q^\mp) p_2(q_i^\pm | Q^\mp, \phi_i^\pm) d\phi_i^\pm \quad (18)$$

where $(\phi_{min}, \phi_{max}) = (-\delta\phi, \pi - \delta\phi)$ for q_i^+ and $(\phi_{min}, \phi_{max}) = (\pi - \delta\phi, 2\pi - \delta\phi)$ for q_i^- . Shown in Fig. 35 are examples of data on the second-order conditional distribution $p_2(q_1^- | Q^+, \phi_1^-)$ which indicate that the mean value of q_1^- computed from p_2 increases with both Q^+ and ϕ_1^- as predicted from the $E - \phi$ diagram.

Shown in Figs. 36 and 37 are additional examples of measured conditional distributions $p_1(\phi_i^- | Q^+)$, $i = 1, 8, 16$ and $p_2(q_1^+ | \phi_1^+, Q^-)$ that again clearly demonstrate the existence of significant memory propagation between successive half-cycles of the applied ac voltage.

The data in Fig. 36 correspond to Trichel-like negative-corona pulses that are known to occur in point-dielectric gaps even at very small gap spacings (1.5 mm). Twenty

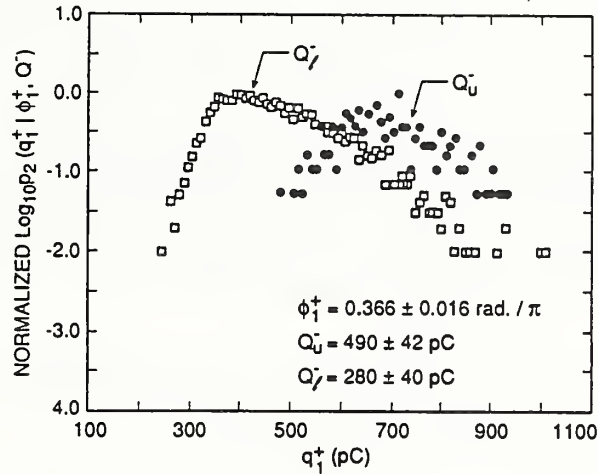


Figure 37. Measured second-order conditional pulse-amplitude distribution of the first pulse in the positive half-cycle. The frequency is 200 Hz, applied voltage is 3.0 kV and gap spacing is 0.0 mm.

or more Trichel pulses could occur in a single half-cycle under the conditions that apply to this figure. Shown in Fig. 36 are both conditional and unconditional phase-of-occurrence distributions for the 1st, 8th, and 16th pulses in the negative half-cycle. The results for $p_1(\phi_{16}^- | Q^+)$ demonstrate that memory of the charge deposited on the dielectric surface by PD on the previous positive half-cycle persists even at the 16th pulse on the negative half-cycle.

The data shown in Fig. 37 correspond to second order conditional amplitude distributions of the first pulse on the positive half-cycle conditioned on the indicated range of values for Q^- and ϕ_1^+ . In this case, the point-to-dielectric gap spacing was 0.0 mm. The behavior is the same as that for $p_2(q_1^- | Q^+, \phi_1^-)$ seen in Fig. 35.

3.2.6 Discussion

The results presented here clearly demonstrate the significance of memory propagation effects in controlling the stochastic behavior of partial discharges generated by an alternating voltage applied to a discharge gap containing a solid dielectric material.

The implications of memory effects revealed here on the interpretation of conditional phase-resolved measurements reported by others [79–81, 84, 92] will now be considered. The unconditional phase-of-occurrence distributions as shown by the dashed lines in Fig. 36 are related to the conditional distributions by an integral

expression similar to Eq. 18, namely

$$p_o(\phi_i^\pm) = \int_o^\infty p_o(Q^\mp) p_1(\phi_i^\pm | Q^\mp) dQ^\mp, \quad (19)$$

where $p_o(Q^\mp) dQ^\mp$ is the probability that the net PD charge in the previous half-cycle will lie in the range Q^\mp to $Q^\mp + dQ^\mp$. For $i > 1$, the occurrence of the i th pulse may depend on previous pulses that occurred in the *same* half-cycle. Taking this into account in the case, for example, of the second pulse gives

$$\begin{aligned} p_o(\phi_2^\pm) &= \int_o^\infty \int_{\phi' - \delta\phi}^{\phi' + \pi} \int_o^\infty p_o(Q^\mp) p_1(\phi_1^\pm | Q^\mp) p_2(q_1^\pm | Q^\mp, \phi_1^\pm) \\ &\times p_3(\phi_2^\pm | Q^\mp, \phi_1^\pm, q_1^\pm) dQ^\mp d\phi_1^\pm dq_1^\pm, \end{aligned} \quad (20)$$

where $\phi' = 0$ or π for positive or negative half-cycles respectively, and a small phase-shift, $\delta\phi$, is introduced to allow for the possibility that a pulse may actually occur slightly before the voltage zero-crossing as is the case for the $i = 1$ data in Fig. 36. Similar, but more complex, integral expressions involving higher-order conditional distributions can be written for $p_o(\phi_i^\pm)$, $i > 2$.

The unconditional phase-resolved distribution of PD events in a particular half-cycle is given by

$$p_o(\phi^\pm \in \Delta\phi^\pm) = \frac{1}{M} \sum_{j=1}^M \sum_{i=1}^N p'_{ij} \int_{\Delta\phi^\pm} p_o(\phi_i^\pm) d\phi_i^\pm, \quad (21)$$

where $p_o(\phi^\pm \in \Delta\phi^\pm) \Delta\phi^\pm$ is the probability that *any* event will occur in the phase interval $\Delta\phi^\pm$, p'_{ij} is the probability that an i th pulse will actually occur in the j th half-cycle, and averages have been performed over M cycles and over the phase window selected. The p'_{ij} can be viewed as weighting factors for the distributions $p_o(\phi_i^\pm)$ such as given by Eq. 20.

The phase-resolved amplitude distribution for the first pulse in a given half-cycle is related to distributions shown in Figs. 36 and 37 by

$$\begin{aligned} p_1(q_1^\pm | \phi_1^\pm \in \Delta\phi^\pm) &= \int_{\Delta\phi^\pm} \int_o^\infty p_o(Q^\mp) p_1(\phi_1^\pm | Q^\mp) \\ &\times p_2(q_1^\pm | Q^\mp, \phi_1^\pm) dQ^\mp d\phi_1^\pm. \end{aligned} \quad (22)$$

More complex integral expressions are found for $i > 1$. The unconditional phase-resolved pulse-height distribution is then given by

$$p(q_i^\pm; \phi_i \in \Delta\phi^\pm)_{i \geq 1} = \frac{1}{M} \sum_{j=1}^M \sum_{i=1}^N p'_{ij} \int_{\Delta\phi^\pm} p_o(\phi_i^\pm) p_1(q_i^\pm | \phi_i^\pm) d\phi_i^\pm. \quad (23)$$

Eqs. 21 and 23 indicate the formidable difficulties to be encountered in the interpretation of unconditional phase-resolved PD data. It can thus be argued from the information presented here that measurement of conditional distributions not only provides more insight into the physics of PD phenomena but may also be more useful for pattern recognition purposes. In general, conditional distributions are more immune to nonstationary behavior than unconditional distributions.

Preliminary results from the measurements reported here have recently been published [93].

4 FAST TRANSIENT MEASUREMENTS

Task 04

Gerald J. FitzPatrick and John E. Lagnese

Electricity Division

National Institute of Standards and Technology

4.1 Introduction

Kerr cells are electro-optic transducers whose optical properties change when high-voltage is applied to them. They have been used at NIST and elsewhere for many years for the measurement of high electric fields and high voltage transients because of their excellent measurement precision [94, 95, 96, 97, 98]. The uncertainty in the voltage determined by Kerr measurements depends upon the errors introduced by the measuring system components such as the light source and detectors, and upon the uncertainty in the determination of the parameter V_m , which is known as the Kerr cell constant. This cell constant is usually determined through simultaneous measurements made with a calibrated voltage divider connected in parallel with the Kerr cell. This report describes the application of curve-fitting techniques to the evaluation of the Kerr cell constant. Previously, such measurements were made with analog oscilloscopes and the cell constant was evaluated by comparing the output intensity of the Kerr measurement system with the voltage divider output at only one point: the voltage peak. The measurements reported here are made with digital recorders which, because of the numerical format of the digitized data, make the comparison between the two measurements over the entire waveform much easier than that formerly done with analog measurements. The results indicate that the fitted values of V_m have much less scatter than the single-point comparisons. The following sections contain a description of the Kerr measurement and curve-fitting technique, a presentation of the results, and a discussion of their significance.

4.2 Kerr Cell Measurements

A typical Kerr cell and major components of the optical detection system are shown in Fig. 38. The system consists of a stabilized laser light source, a Kerr cell with polarizers at its input and output, a light detector for optical/electrical conversion, and a digital voltage recorder to measure the detector output. The Kerr cell itself is essentially a parallel plate capacitor connected to the high voltage circuit at the point where the voltage is to be measured. When high voltage is applied to the electrodes of the cell, the electric field between them induces a birefringence in the

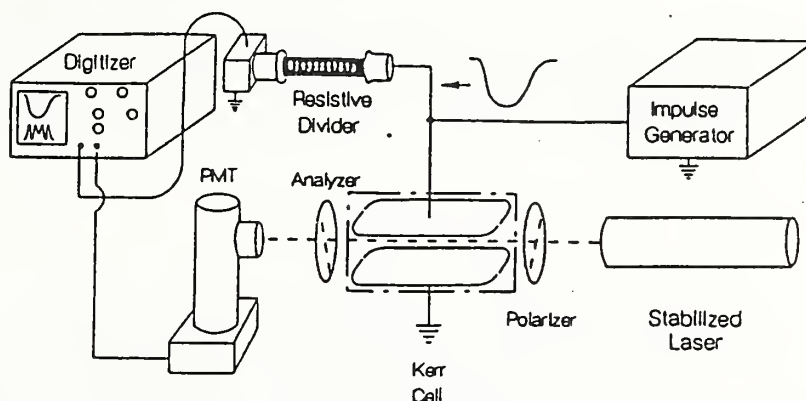


Figure 38. Kerr cell measurement system including laser, polarizers, photomultiplier tube (PMT), and digitizer. A resistive voltage divider is shown connected in parallel to the Kerr cell.

Kerr liquid in the direction parallel to the field and that perpendicular to it. The relation of the measured output light intensity I to the applied voltage V for an ideal Kerr measurement system having polarizers oriented at $\pm 45^\circ$ to the direction of the field within the Kerr cell is given by [99]:

$$I/I_m = \sin^2\left(\frac{\pi}{2}\left(\frac{V}{V_m}\right)^2\right). \quad (24)$$

I_m is the light intensity at maximum transmission. The cell constant, V_m , is defined as:

$$V_m = \frac{d}{\sqrt{2Bl'}}, \quad (25)$$

where B is the electro-optic Kerr coefficient, d is the electrode spacing, and l' is the effective electrode length. The output intensity of the Kerr measurement system for an applied impulse voltage is shown in Figs. 39a and 39b. The output intensity shown in the figure and defined by Eq. (24) passes through a number of maxima and minima called fringes as the applied voltage increases. The fringe number n is defined as the ratio $(V/V_m)^2$. If the cell constant is known, then the voltage can be determined from the Kerr cell intensity measurement by solving Eq. (24). The result can then be used to calibrate a voltage divider through measurements made simultaneously with the Kerr cell connected in parallel to the divider.

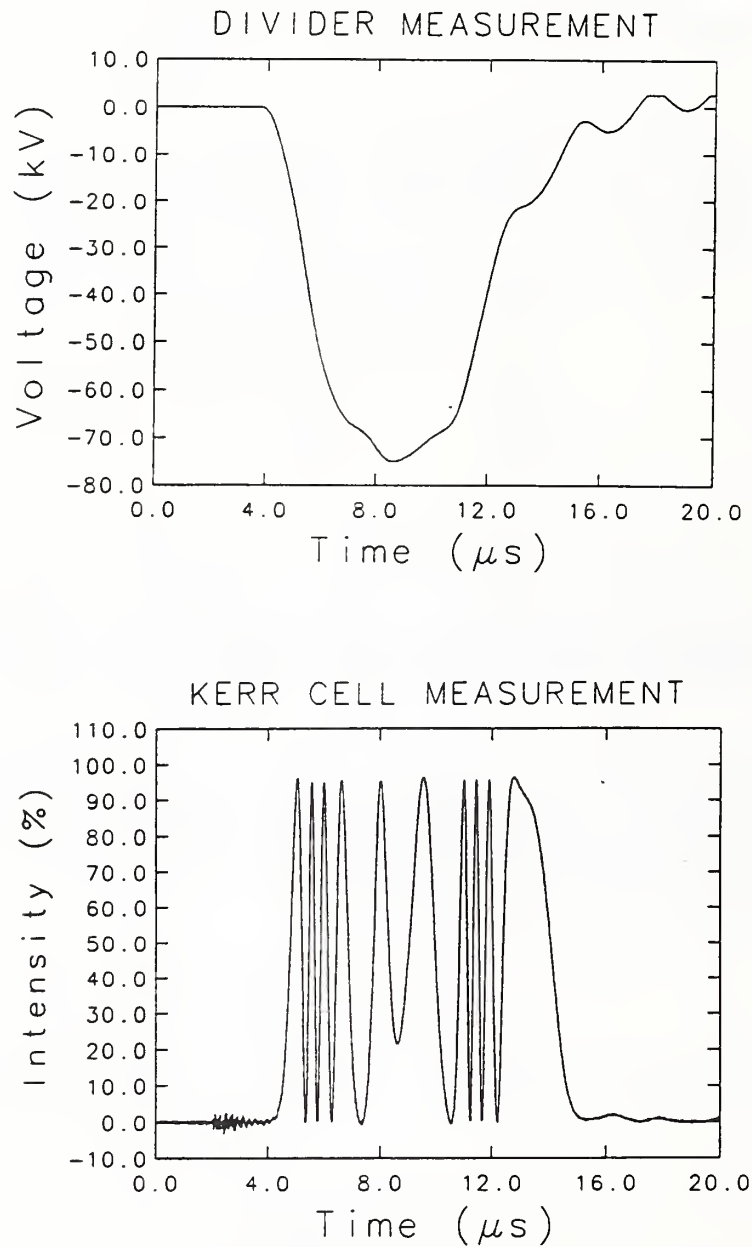


Figure 39. Simultaneous measurements made with (a) a resistive voltage divider and (b) a Kerr cell connected in parallel.

4.3 Kerr Cell Constant Determination

The Kerr cell and a known voltage divider are connected in parallel to the high-voltage impulse generator as shown in Fig. 38. The voltage divider provides a scaled replica of the high-voltage waveform applied to it. The high voltage, V , is related to the divider output, v_{out} , by:

$$V = D \cdot v_{out}, \quad (26)$$

where D is the divider ratio, which ideally is a constant. Eq. (24) is then fitted to the measured Kerr output intensity using the voltage determined from the divider output voltage with Eq. (26). Analog measurements have previously been used to determine Kerr cell constants with an estimated relative uncertainty of 0.3% (1σ) in the measurement of the peak voltage [100].

For the digital measurements, the following method is used for fitting the measured curves. Given data pairs (V_i, I_i) for $i=1, \dots, M$, we consider the problem of fitting a model $y(V; \mathbf{p})$ to the data; \mathbf{p} is the vector of the unknown parameters. The problem is to compute estimates of those parameters which minimize the quantity Q over a suitable region, where Q is given by:

$$Q = \sum_{i=1}^M \{I_i - y(V_i; \mathbf{p})\}^2. \quad (27)$$

The algorithm employed to estimate the optimal values of the parameters is a modification of the Levenberg-Marquardt algorithm, which is an iterative search procedure for finding the minimum value of the sum-of-the-squares of M nonlinear functions in N variables. It is essentially a combination of the Gauss-Newton and steepest-descent methods, and is designed to avoid both the divergence problems associated with the Gauss-Newton algorithm and also the progressively slower convergence frequently encountered in the steepest-descent method. The starting point in the search is determined by initial estimates of the optimal parameters. A new search direction is chosen by a suitable interpolation between the search directions provided by the two algorithms. At points where the objective function, Q , is rapidly changing (usually these are far from the optimal solution), the search direction is close to that provided by the method of steepest descent. Near the optimal solution, where the gradient of the objective function is small and the function is approximately linear, the search direction is close to that provided by the Gauss-Newton method.

Another feature of the Levenberg-Marquardt algorithm, as implemented in the public-domain software package employed in this study [101], is the use of implicitly-scaled variables in order to achieve scale invariance of the method and to limit the size of the correction in any direction where the objective function is changing rapidly. Under

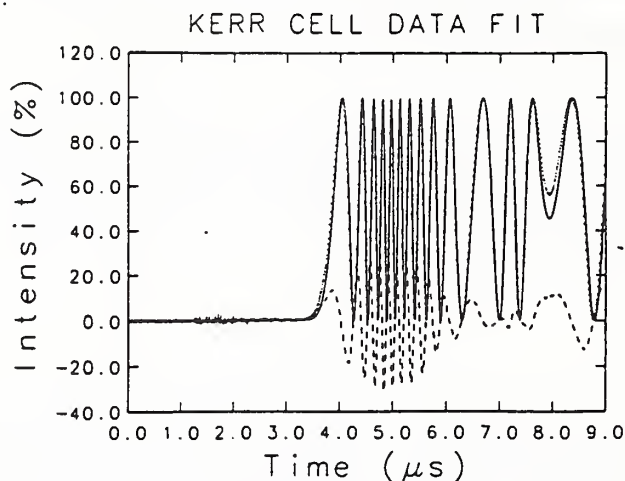


Figure 40. Measured and fitted Kerr intensities for ϕ and V_o set to zero. The measured intensity appears as individual points. The fitted intensity curve is the solid curve. The difference of the two intensities is shown as the dashed curve.

reasonable conditions on the objective function, this optimal choice of the correction enhances global convergence from starting points far from the solution and has a fast rate of convergence for problems with small residuals.

The available data consisted of 2048 measurements of V_i and I_i , with each data pair simultaneously measured at equally-spaced time samples taken at 10 ns intervals. The V_i are the voltages measured with the voltage divider and the I_i are the corresponding intensities measured with the Kerr cell system connected in parallel with the divider. To eliminate the effects of random noise in the V_i measurements, these data were smoothed using a least-squares cubic-spline fit with 100 equally-spaced knots. The smoothed voltages were those used in Eq. (28) to obtain the fits shown in Figs. 40 and 41. An examination of the residuals between the measured and smoothed voltages showed that the fitting procedure had the desired effect of removing the random noise without distorting the voltage waveform. Fig. 42 demonstrates the result of using the noisy voltage data when fitting Eq. (28) to intensity data under the conditions shown in Fig. 41. The rms error of the difference of the fitted and measured curves is reduced by about half when the voltage data are smoothed.

The model used in this study for fitting of the measured Kerr waveforms is a modification of Eq. (24):

$$I = I_m \sin^2 \left[\frac{\pi}{2} \left(\frac{V - V_o}{V_m} \right)^2 + \phi \right] + I_o. \quad (28)$$

The phase angle, ϕ , in this equation is used to account for constant birefringences in the Kerr measurement system, such as those produced by stress in the glass

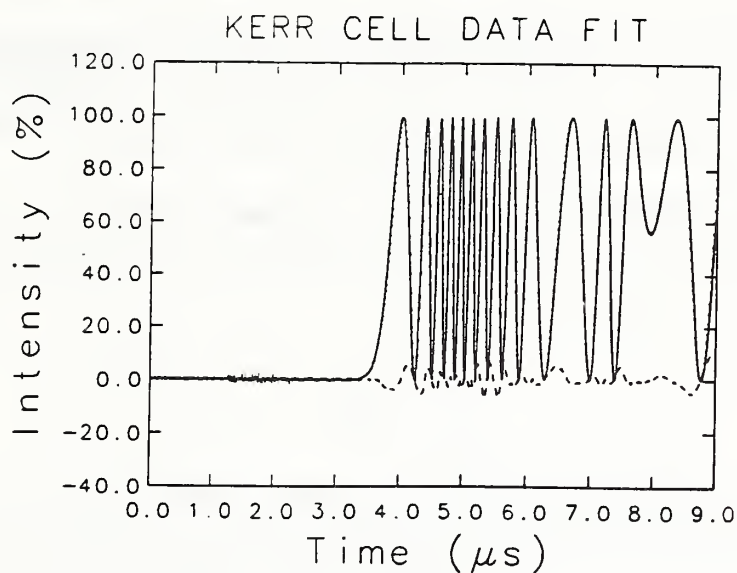


Figure 41. Measured and fitted Kerr intensities for fitted V_0 . The measured intensity appears as individual points; the fitted intensity curve is the solid curve. The difference between the two intensities is shown as the dashed curve.

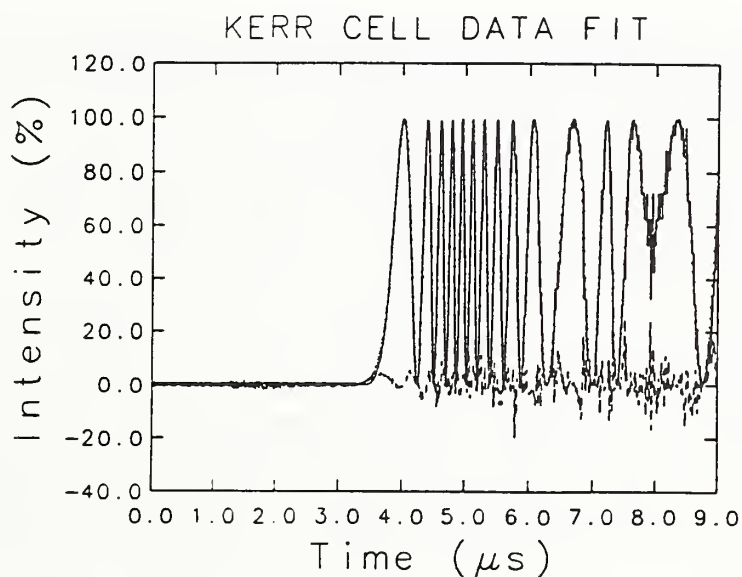


Figure 42. Kerr intensity curve found using unsmoothed voltage data. The measured intensity appears as individual points; the fitted intensity curve is the solid curve. The difference between the two intensities is shown as the dashed curve.

windows of the Kerr cell. Eq. (28) also contains a term, I_o , to account for background light intensity in the measurements. This term arises from room light entering the photodetector and from nonideal polarizers that may pass a small amount of light even when their axes are orthogonally aligned.

The single-point estimate that has been used in the past to calculate the cell constant from the peak voltage, V_p , using analog measurements of the Kerr intensity and divider output is :

$$V_m = \frac{V_p - V_o}{\sqrt{n_p}}. \quad (29)$$

The peak voltage, V_p , is determined from the voltage divider measurement and from n_p , which is the Kerr fringe number corresponding to the voltage peak. The voltage offset, V_o , is found from the divider data and is usually taken as the average of several hundred data points preceding the rise of the voltage impulse. In this study, the value of V_o found from fitting Eq. (28) to the Kerr waveform was used for the single-point calculation, Eq. (29).

4.4 Results and Discussion

The function given in Eq. (28), was used to fit the measured intensity curves to a point slightly beyond that corresponding to the peak voltage. Initially, the curve-fitting was performed with only the adjustable parameters for the intensity maximum, I_m , intensity offset, I_o , and cell constant V_m ; the phase angle, ϕ , and offset voltage, V_o , were set to zero. A typical curve fit using only these parameters is shown in Fig. 40. Fitting the phase angle, ϕ , resulted in fits that were somewhat better: the mean differences between fitted and measured curves and the total rms error were reduced. The values determined for the fitted phase angle were small, as was expected since this parameter accounts for fixed birefringences in the optical measurement system. These birefringences, such as stress birefringence in the cell windows, have been found in other investigations to be small [102]. When the offset voltage, V_o , was fitted and ϕ was set to zero, further improvements in the fits were realized, as shown in Fig. 41. The differences between the fitted and measured curves were in the worst case less than 5% of I_m and the rms error was reduced to less than half of that when V_o was not a fitted parameter.

It is useful to compare the fitted values of V_m to those estimated from the single-point V_p as described in the previous section, Eq. (29). The results given in Table 7 show that the scatter in the value of V_m is reduced by an order of magnitude over that resulting from the calculated single-point values. These values were determined as the average of V_m determined from fits using impulse voltage waveforms having peak voltages over a range from $1.73 V_m$ (3.5 fringes) to $5.96 V_m$ (35.5 fringes). The error

Table 7. Kerr cell constants found with curve-fitting technique and calculated at a single point.

Polarizer Position	$V_{m,fit}(V)$	$V_{m,calc}^*(V)$
Orthogonally aligned	19 530±30	19 470±360
Misadjusted	19 520±40	19 583±470

All numbers reported are 3σ

Values are temperature-corrected to 22.6°C

* corrected for voltage offset

reported in the table represents three standard deviations ($\pm 3\sigma$). It should also be noted that the comparison of V_m 's also includes a correction for temperature, since the data were taken at slightly different temperatures and the cell constant varies with temperature. The temperature correction method has been reported elsewhere [103]. The V_m 's reported in Table 1 are all corrected to 22.6°C. The largest differences between the fitted and the measured curves, as shown in Fig. 41, typically occur at the points midway between the minimum and maximum intensities, where the intensity changes most rapidly with the voltage.

The values of the fitted and calculated cell constants for fringe numbers, n_p , between 3.5 and 35.5 are shown in Fig. 43. The fringe number n_p is an indicator of the peak voltage, since they are related through Eq. (29). The V_m 's determined from the fitted curves are essentially independent of the fringe number. The corrected single-point estimates of V_m fall below the fitted values at low fringe number, but the two curves converge to nearly the same value for fringe numbers greater than 25. This dependence of the values of the calculated V_m 's on fringe number is in agreement with theory, which predicts that the random error $\delta V_m/V_m$ is:

$$\frac{\delta V_m}{V_m} = \left[\left(\frac{\delta V}{V} \right)^2 + \left(\frac{\delta n}{n} \right)^2 \right]^{1/2}. \quad (30)$$

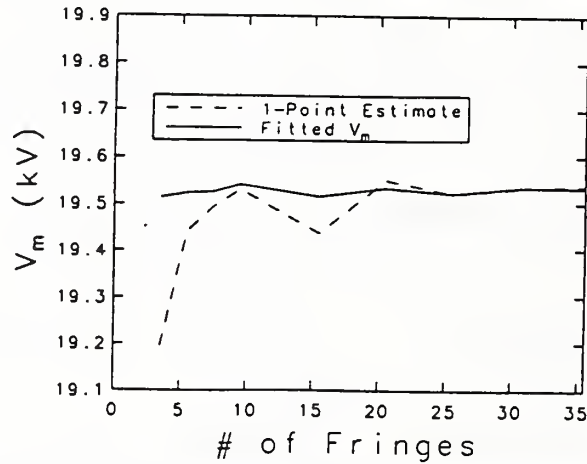


Figure 43. Dependence of fitted and calculated values for the Kerr cell constant V_m on fringe number corresponding to the peak voltage, n_p .

The relative error $\delta V/V$ in the measured output voltage from the divider is approximately constant while the relative error $\delta n/n$ in fringe number decreases with increasing n . According to Eq. (30), the random error in the calculated V_m also decreases as the fringe number increases. This is characteristic of Kerr cell measurements: their sensitivity increases with increasing voltage. The sensitivity of the fitting technique to changes in the relative position of the axes of the polarizers was also investigated and the results are given in Table 1. For this test, the polarizers were rotated relative to each other so that they were no longer oriented orthogonally, but misaligned by approximately 9° . There is excellent agreement between the values of the fitted V_m determined from measurements with orthogonally-aligned polarizers and with slightly misaligned polarizers. The scatter is small for both cases. The change in the calculated single-point estimate is greater than for the fitted value of V_m , but the differences fall within 1σ for both the fitted and calculated V_m 's. The results indicate that the fitting technique is insensitive to small misalignments of the polarizers.

In another test, the same cell was filled with a different Kerr liquid, *o*-dichlorobenzene, and the cell constant, V_m , was again evaluated using the curve-fitting software. With nitrobenzene, the cell constant, V_m , reported in Table 1 is 19530 ± 30 V. The fitted cell constant, V_m , with *o*-dichlorobenzene was 43470 ± 780 V. These cell constants are evaluated by fitting a section of the Kerr output waveform, typically from the time at the start of the pulse to a time slightly greater than that corresponding to the peak voltage, as shown in Fig. 41. The V_m found from fitting the first half of the waveform, from start to the voltage peak was found to differ from that found from the latter half of the waveform (from voltage peak to zero) by as much as 1-2% for the *o*-dichlorobenzene data. The scatter is also considerably greater in the fitted V_m , but this may be due to the range of fringes over which this average is taken, which

for the o-dichlorobenzene data extended from 3.2 to 7.5 fringes. The significance of the difference in V_m , depending upon which segment of the waveform is fitted, is also unclear due to the large scatter in the data. Further measurements at higher fringe number are required to reduce this variation.

The reduced scatter in the fitted V_m 's was achieved by fitting the voltage offset V_o in Eq. (28). The best-fit offsets were, however, considerably higher than expected. The voltage offset is ordinarily removed from the voltage waveform during preprocessing by subtracting the mean of several hundred data points prior to the start of the voltage pulse from the entire waveform. It was therefore expected that the fitted V_o should be small, perhaps of the order of $0.02 V_m$. The actual values were $0.08 V_m$ to $0.1 V_m$, and at the highest voltages, $0.01 V_p$ to $0.02 V_p$. The single-point estimates, when corrected for voltage offset according to Eq. (29), were in excellent agreement with the fitted V_m 's, as shown in Table 1. However, the uncorrected single-point estimates differed from the fitted V_m 's by as much as 1–2%, but this difference still falls within the scatter. The voltage correction term, V_o , in addition to accounting for any residual offset in the voltage waveform, may also compensate for small timing delays between the voltage and intensity waveforms. For an ideal ramp voltage, a voltage offset is equivalent to a time delay. The voltage pulses used in this study rise monotonically to V_p and can be approximated by a voltage ramp. Also, the effect of including a voltage offset in Eq. (28) is equivalent to introducing a voltage-dependent phase angle (with or without the fixed phase angle ϕ). This can be seen if the $(V - V_o)^2$ term is expanded:

$$I = I_m \sin^2 \left[\frac{\pi}{2} \left(\frac{V}{V_m} \right)^2 + \alpha V + \beta \right] + I_o \quad (31)$$

with:

$$\alpha = \frac{-\pi V_o}{V_m^2}$$

$$\beta = \frac{\pi}{2} \left(\frac{V_o}{V_m} \right)^2 + \phi$$

Further studies are being undertaken to determine the significance of the correction term, V_o , and also to investigate the systematic errors in the determination of the cell constant with both the curve-fitting and single-point estimates.

4.5 Conclusions

Preliminary results using the curve-fitting technique described in this paper indicate that this approach may reduce the uncertainties in the determination of the Kerr cell constants using comparative digitized measurements. The Kerr cell constants

resulting from the curve-fitting technique had much smaller variation with peak voltage than did the corresponding single-point estimates; the standard deviation of the fitted cell constants was an order of magnitude smaller than that for the calculated single-point values over a wide range of voltages. The best fits to the measured Kerr waveforms were attained when a constant correction term to the voltage in the Kerr equation was included. The correction term was larger than expected and the significance of this correction will be further investigated. In the past, analog measurements have been limited to evaluating the cell constant only at single points, typically at the peak of the voltage impulse. It is only with digitized measurements that the use of curve-fitting techniques such as the one described in this paper are possible.

5. REFERENCES

- [1] M. Misakian, "In Vitro Exposure Parameters With Linearly and Circularly Polarized ELF Magnetic Fields", *Bioelectromagnetics*, **12**, pp. 377-381 (1991).
- [2] M. Misakian and W.T. Kaune, "An Optimum Experimental Design For In Vitro Studies Using ELF Magnetic Fields", *Bioelectromagnetics*, **11**, pp. 251-255 (1990).
- [3] B.R. McLeod, A.A. Pilla, and M.W. Sampsel, "Electromagnetic Fields Induced by Helmholtz Aiding Coils Inside Saline-Filled Boundaries", *Bioelectromagnetics*, **4**, pp. 357-370 (1983).
- [4] M. Misakian, W.E. Anderson, and O.B. Laug, "Drift Tubes for Characterizing Atmospheric Ion Mobility Spectra Using AC, AC-Pulse, and Pulse Time-of-Flight Measurement Techniques", *Rev. Sci. Instrum.*, **60**, pp. 720-729 (1989).
- [5] M. Misakian, "Generation and Measurement of DC Electric Fields With Space Charge", *J. Appl. Phys.*, **52**, pp. 3135-3144 (1981).
- [6] R.H. McKnight, F.R. Kotter and M. Misakian, "Measurement of Ion Current Density At Ground Level In The Vicinity of High Voltage DC Transmission Lines", *IEEE Trans. Power Appar. Systems*, **PAS-102**, pp. 934-941 (1987).
- [7] M. Misakian, R.H. McKnight and C. Fenimore, "Calibration of Aspirator-type Ion Counters and Measurement of Unipolar Charge Densities", *J. Appl. Phys.*, **61**, pp. 1276-1287 (1987).
- [8] G.E. Spangler and J.P. Carrico, "Membrane Inlet For Ion Mobility Spectrometry (Plasma Chromatography)", *Int. J. Mass. Spectrom. Ion Phys.*, **52**, pp. 267-287 (1983).
- [9] F.Y. Chu, I. Sauers, and G.D. Griffin, "A Review of the Formation of S_2F_{10} in Gas Insulated Equipment," *Conf. Rec.-1988 IEEE Int. Symp. on Elec. Insul.*, IEEE publication **88-CH2594-0-DEI**, pp. 131-134, (1988).
- [10] I. Sauers, G. Harman, J.K. Olthoff, and R.J. Van Brunt, " S_2F_{10} Formation by Electrical Discharges in SF_6 : Comparison of Spark and Corona," in *Gaseous Dielectrics VI, Proc. 6th Int. Symp. on Gaseous Dielectrics*, Plenum Press, New York, pp. 553-562, (1991).
- [11] G.D. Griffin, M.S. Ryan, K. Kurka, M.G. Nolan, I. Sauers, and D.R. James, "Disulfur Decafluoride (S_2F_{10}): A Review of the Biological Properties and Our Experimental Studies of This Breakdown Product of SF_6 ," in *Gaseous Dielectrics VI, Proc. 6th Int. Symp. on Gaseous Dielectrics*, Plenum Press, New York, pp. 545-552, (1991).

-
- [12] J.T. Herron, "A Critical Review of the Chemical Kinetics of SF₄, SF₅, and S₂F₁₀ in the Gas Phase," *Int. J. Chem. Kinetics*, **19**, pp. 129–142 (1987).
- [13] R.J. Van Brunt and J.T. Herron, "Fundamental Processes of SF₆ Decomposition and Oxidation in Glow and Corona Discharges," *IEEE Trans. Elec. Insul.*, **25**, pp. 75–94, (1990).
- [14] R.J. Van Brunt, J.T. Herron, and C. Fenimore, "Corona-Induced Decomposition of Dielectric Gases," in *Gaseous Dielectrics V, Proc. 5th Int. Symp. on Gaseous Dielectrics*, Pergamon Press, New York, pp. 163–173, (1987).
- [15] J.K. Olthoff, R.J. Van Brunt, J.T. Herron, I. Sauers, and G. Harman, "Catalytic Decomposition of S₂F₁₀ and Its Implications on Sampling and Detection from SF₆-Insulated Equipment," *Conf. Rec.-1990 IEEE Int. Symp. on Elec. Insul.*, IEEE publication 90-CH2727-6, pp. 248–252, (1990).
- [16] J.K. Olthoff, R.J. Van Brunt, J.T. Herron, and I. Sauers, "Detection of Trace Disulfur Decafluoride in Sulfur Hexafluoride by Gas Chromatography/Mass Spectrometry," *Anal. Chem.*, **63**, pp. 726–732, (1991).
- [17] R.J. Van Brunt, "Production Rates for Oxyfluorides SOF₂, SO₂F₂, and SOF₄ in SF₆ Corona Discharges," *J. Res. National Bureau of Standards*, **90**, pp. 229–253, (1985).
- [18] F.J.J.G. Janssen, "Measurement at the sub-ppm Level of Sulphur-Fluoride Compounds Resulting from the Decomposition of SF₆ by Arc Discharge," *Kema Scientific & Technical Report*, **2**, pp. 9–18, (1984).
- [19] R.J. Van Brunt, L.W. Sieck, I. Sauers, and M.C. Siddagangappa, "Transfer of F⁻ in the Reaction of SF₆⁻ with SOF₄: Implications for SOF₄ Production in Corona Discharges," *Plasma Chem. Plasma Proc.*, **8**, pp. 225–246, (1988).
- [20] A. Stamatovic and G.J. Schulz, *Rev. Sci. Instrum.* **41**, 423 (1970); M. R. McMillan and J. H. Moore, *ibid.* **51**, 944 (1980); G. J. Schulz, *Phys. Rev. A* **5**, 1672 (1972).
- [21] H.-X. Wan, J.H. Moore, and J.A. Tossell, *J. Chem. Phys.* **91**, 7340 (1989).
- [22] H.-X. Wan, J.H. Moore, and J.A. Tossell, *J. Chem. Phys.* **94**, 1868 (1991).
- [23] A.R. Johnston and P.D. Burrow, *J. Electron Spectrosc. Relat. Phenom.* **25**, 119 (1982).
- [24] R.E. Kennerly, R.A. Bonham, and M. McMillan, *J. Chem. Phys.* **70**, 2039 (1979).
- [25] M.S. Dababneh, Y.-F. Hsieh, W.E. Kaupilla, C.K. Kwan, S.J. Smith, T.S. Stein, and M.N. Uddin, *Phys. Rev. A* **38**, 1207 (1988).

-
- [26] J. Ferch, W. Raith, and K. Schröder, *J. Phys. B: At. Mole. Phys.* **15**, L175 (1982).
- [27] F.C. Fehsenfeld, *J. Chem. Phys.* **53**, 2000 (1970).
- [28] P.J. Hay, *J. Chem. Phys.* **76**, 502 (1982).
- [29] L.G. Christophorou, D.L. McCorkle, and J.G. Carter, *J. Chem. Phys.* **54**, 253 (1971); D.L. McCorkle, A.A. Christodoulides, L.G. Christophorou, and I. Szamrej, *ibid* **72**, 4049 (1980).
- [30] M. Fenzloff, R. Gerhard, and E. Illenberger, *J. Chem. Phys.* **88**, 149 (1988).
- [31] A. Chutjian and S.H. Alajajian, *Phys. Rev. A* **31**, 2885 (1985); O. J. Orient and A. Chutjian, *ibid.* **34**, 1841 (1986).
- [32] L.E. Kline, D.K. Davis, C.L. Chen, and P.J. Chantry, *J. Appl. Phys.* **50**, 6789 (1979).
- [33] D. Rapp and P. Englander-Golden, *J. Chem. Phys.* **43**, 1464 (1965).
- [34] S.R. Hunter, J.G. Carter, and L.G. Christophorou, *J. Chem. Phys.* **90**, 4879 (1989).
- [35] R.W. Odom, D.L. Smith, and J.H. Futrell, *J. Phys. B* **8**, 1349 (1975); J.E. Delmore, and L.D. Appelhans, *J. Chem. Phys.* **84**, 6238 (1986).
- [36] Y. Wang, R.L. Champion, L.D. Doverspike, J.K. Olthoff, and R.J. Van Brunt, *J. Chem. Phys.* **91**, 2254 (1989).
- [37] A.V. Phelps and R.J. Van Brunt, *J. Appl. Phys.* **64**, 4269 (1988).
- [38] J.P. Novak and M.F. Fréchette, *J. Appl. Phys.* **55**, 107 (1984).
- [39] T. Yoshizawa, Y. Sakai, H. Tagashira, and S. Sakamoto, *J. Phys. D: Appl. Phys.* **12**, 1839 (1979).
- [40] C. Szmytkowski and K. Maciag, *Chem. Phys. Lett.* **124**, 463 (1986).
- [41] M. Zubek, S. Kadifachi and J.B. Hasted, in *Book of Abstracts of the European Conference on Atomic Physics*, eds. J. Kowalski, G. zu Putlitz and H.G. Weber p. 763, (Heidelberg, 1981).
- [42] V.F. Sokolov and Y.A. Sokolova, *Soviet Tech. Phys. Lett.* **7**, 268 (1981).
- [43] O.J. Orient, I. Iger, and S K. Srivastava, *J. Chem. Phys.* **77**, 3523 (1982).
- [44] O.J. Orient and S.K. Srivastava, *J. Chem. Phys.* **80**, 140 (1984).
- [45] L. Vušković and S. Trajmar, *J. Chem. Phys.* **77**, 5436 (1982).

-
- [46] L. Sanche and G.J. Schulz, *J. Chem. Phys.* **58**, 79 (1973).
- [47] L. Andrić, I.M. Čadež, R.I. Hall, and M. Zubek, *J. Phys. B: At. Mol. Phys.* **16**, 1837 (1983).
- [48] I.M. Čadež, V.M. Pejčev, and M.V. Kurepa, *J. Phys. D: Appl. Phys.* **16**, 305 (1983).
- [49] O.J. Orient and S.K. Srivastava, *J. Chem. Phys.* **78**, 2949 (1983).
- [50] S.M. Spyrou, I. Sauers, and L.G. Christophorou, *J. Chem. Phys.* **84**, 239 (1986).
- [51] J. Rademacher, L.G. Christophorou, and R.P. Blaunstein, *J. Chem. Soc. Faraday Trans. II*, **71**, 1212 (1975).
- [52] G.H. Dunn, *Phys. Rev. Letters* **8**, 62 (1962).
- [53] T.F. O'Malley and H.S. Taylor, *Phys. Rev.* **176**, 207 (1968).
- [54] R.J. Van Brunt and L.J. Kieffer, *Phys. Rev. A* **2**, 1899 (1970).
- [55] J.A. Tossell, *Chem. Phys.*, **154**, 211 (1991).
- [56] A. Benitez, J.H. Moore and J.A. Tossell, *J. Chem. Phys.*, **88**, 6691 (1988).
- [57] I. Sauers, L.G. Christophorou, and S.M. Spyrou, in *Gaseous Dielectrics IV* (L. G. Christophorou and M. O. Pace, Eds.), Pergamon Press, New York, pp. 261–272 (1984).
- [58] J.S. Wang and J.L. Franklin, *Int. J. Mass. Spectrom. Ion Phys.* **36**, 233 (1980).
- [59] P.G. Datskos and L.G. Christophorou, *J. Chem. Phys.* **90**, 2626 (1989).
- [60] P.W. Harland and J.C.J. Thynne, *J. Phys. Chem.* **75**, 3517 (1971).
- [61] L.M. Babcock and G.E. Streit, *J. Phys. Chem.* **86**, 1240 (1982).
- [62] T.M. Miller, A.E.S. Miller, and X. Liu, *Abstracts of Contributed Papers, 17th International Conference on the Physics of Electronics and Atomic Collisions*, (I.E. McCarthy, W.R. MacGillivray, M.C. Standage, Eds.), p. 260 (1991).
- [63] R.J. Van Brunt and M.C. Siddagangappa, *Plasma Chem. Plasma Proc.* **8**, 207 (1988).
- [64] A. Derdouri, J. Casanovas, R. Hergli, R. Grob, and J. Mathieu, *J. Appl. Phys.* **65**, 1852 (1989).
- [65] I. Sauers, *Plasma Chem. Plasma Proc.* **8**, 247 (1988).
- [66] C.L. Chen and P.J. Chantry, *J. Chem. Phys.* **71**, 3897 (1979).

-
- [67] J.W. Gallagher, E.C. Beaty, J. Dutton and L.C. Pitchford, "An Annotated Compilation and Appraisal of Electron Swarm Data in Electronegative Gases" *J. Phys. Chem. Ref. Data*, **12**, 109–152, (1983).
- [68] G.J. FitzPatrick, P.J. McKenny and E.O. Forster, "The effect of pressure on streamer inception and propagation in liquid hydrocarbons," *IEEE Trans. Electric Insul.* **EI-25**, 672–682 (1990).
- [69] R.E. Hebner, E.F. Kelley, E.O. Forster and G.J. FitzPatrick, "Observation of prebreakdown and breakdown phenomena in liquid hydrocarbons," *J. Electrostatics*, **12**, 265–283 (1982).
- [70] E.F. Kelley, R.E. Hebner, G.J. FitzPatrick and E.O. Forster, "The effect of pressure on streamer initiation in n-hexane" *Conf. Record, 1986 IEEE Intl. Symp. Electr. Insul.*, pp 66–68 (1986).
- [71] G.J. FitzPatrick, E.O. Forster, R.E. Hebner and E.F. Kelley, "Prebreakdown cathode processes in liquid hydrocarbons," *IEEE Trans. Electr. Insul.* **EI-22**, 453–458 (1987).
- [72] E.O. Forster, "Progress in the understanding of electrical breakdown in condensed matter," *J. Phys. D: Appl. Phys.*, **23**, 1506–1514 (1990).
- [73] P.K. Watson and W.G. Chadband, "The dynamics of prebreakdown cavities in viscous silicone fluids in negative point-plane gaps," *IEEE Trans. Electr. Insulation*, **EI-23**, 729–738 (1988).
- [74] K.L. Stricklett, E.F. Kelley, H. Yamashita, C. Fenimore, M.O. Pace, T.V. Blalock, A.L. Wintenberg and I. Alexeff, "Observation of Partial discharges in hexane under high magnification," *IEEE Trans. Electr. Insul.*, **EI-26**, 692–698 (1991).
- [75] E.O. Forster, C. Mazzetti and M. Pompili, "The effect of molecular structure on the properties of dielectric fluids," *IEEE Trans. Electr. Insul.*, **EI-26**, 749–754 (1991).
- [76] A.L. Fetter and J.D. Walecka, *Theoretical Mechanics of Particles and Continua*, chap. 9, McGraw-Hill, New York, NY, (1980).
- [77] P.J. McKenny and P.B. McGrath, "Anomalous Positive Point Prebreakdown Behavior in Dielectric Liquids," *IEEE Transactions on Electrical Insulation*, Vol. **EI-19**, No. 2, April, (1984).
- [78] K.L. Stricklett, E.F. Kelley, H. Yamashita, H. Kawai, and C. Fenimore, "Electrical Breakdown and Streamer Statistics in N-Hexane under Uniform Field Conditions," *1990 IEEE International Symposium on Electrical Insulation*, pp. 61–64.

-
- [79] E. Gulski, P.H.F. Morshuis, and F.H. Kreuger, "Atomized Recognition of Partial Discharges in Cavities," *Japanese J. Appl. Phys.*, Vol. 29, pp. 1329–1335, (1990).
- [80] E. Gulski and F.H. Kreuger, "Computer-aided Analysis of Discharge Patterns," *J. Phys. D: Appl. Phys.*, Vol. 23, pp. 1569–1575, (1990).
- [81] T. Okamoto and T. Tanaka, "Novel Partial Discharge Measurement-Computer-Aided Measurement Systems," *IEEE Trans. Elec. Insul.*, Vol. EI-21, pp. 1015–1016, (1986).
- [82] N. Hozumi, T. Okamoto, and H. Fukagawa, "Simultaneous Measurement of Microscopic Image and Discharge Pulses at the Moment of Electrical Tree Initiation," *Jpn. J. Appl. Phys.*, Vol. 27, pp. 572–576, (1988).
- [83] U. Bammert and M. Beyer, "Partial Discharges Measured with an Automated System in Epoxy Resin and Polyethylene," *IEEE Trans. Elect. Insul.*, Vol. 23, pp. 215–225, (1988).
- [84] M. Hikita, K. Yamada, A. Nakamura, T. Mizutani, A. Oohasi, and M. Ieda, "Measurements of Partial Discharges by Computer Analysis of Partial Discharge Distribution by the Monte Carlo Method," *IEEE Trans. Elect. Insul.*, Vol. 25, pp. 453–468, (1990).
- [85] J. Fuhr, M. Haessig, B. Fruth, and T. Kaiser, "PD-Fingerprints of Some High Voltage Apparatus," *Conf. Rec. 1990 IEEE Int. Symp. on Elect. Insul.*, IEEE, New York, pp. 129–132, (1990).
- [86] T. Ito, M. Ito, Y. Ehara, H. Kishida, K. Jogan, and M.S.A.A. Hamman, "Statistical Analysis of Partial Discharge Aging of Insulating Materials," *1990 Annual Report - Conf. on Elect. Insul. and Dielectric Phenomena*, IEEE Pub. 90CH2919-9, pp. 337–342, (1990).
- [87] T. Okamoto and T. Tanaka, "Novel Partial Discharge Measurement Computer-Aided Measurement Systems," *IEEE Trans. Elect. Insul.*, Vol. EI-21, pp. 1015–19016, (1986).
- [88] R.J. Van Brunt, "Stochastic Properties of Partial-Discharge Phenomena," *IEEE Tran. Elec. Insul.*, Vol. 26, Oct., (1991).
- [89] R.J. Van Brunt and S.V. Kulkarni, "Stochastic Properties of Trichel-Pulse Corona: A Non-Markovian Random Point Process," *Phys. Rev. A*, Vol. 42, pp. 4908–4932, (1990).
- [90] R.J. Van Brunt and S.V. Kulkarni, "Method for Measuring the Stochastic Properties of Corona and Partial-Discharge Pulses," *Rev. Sci. Instrum.*, Vol. 60, pp. 3012–3023, (1989).

-
- [91] R.J. Van Brunt, M. Misakian, S.V. Kulkarni, and V.K. Lakdawala, "Influence of a Dielectric Barrier on the Stochastic Behavior of Trichel-pulse Corona," *IEEE Trans. Elec. Insul.*, Vol. 26, pp. 405-415, (1991).
- [92] J.M. Braun, S. Rizzetto, N. Fujimoto, and G.L. Ford, "Modulation of Partial Discharge Activity in GIS Insulators by X-ray Irradiation," *IEEE Trans. Elect. Insul.*, Vol. 26, pp. 460-468, (1991).
- [93] R.J. Van Brunt and E.W. Cernyar, "Influence of Memory Propagation on Phase-Resolved Stochastic Behavior of AC-Generated Partial Discharges," *Appl. Phys. Lett.*, Vol. 48, pp. 2628-2630, (1991).
- [94] E.F. Kelley and R.E. Hebner, Jr., "Electro-Optic Measurement of the Electric Field Distribution in Transformer Oil," *1978 Annual Report, Conference on Electrical Insulation and Dielectric Phenomena*, ISBN #0-309-02861-2, pp. 206-212, (1978).
- [95] R.E. Hebner, Jr., E.C. Cassidy, and J.E. Jones, "Improved Techniques for the Measurement of High-Voltage Impulses Using the Electro-Optic Kerr Effect," *IEEE Trans. Inst. Meas.*, IM-24, no. 4, pp. 361-366, December, (1975).
- [96] M. Zahn, and T. Takada, "High voltage electric field and space-charge distributions in highly purified water," *J. Appl. Phys.*, 54, no. 9, pp. 4762-4775, September, (1983).
- [97] J.D. Cross and R. Tobazeon, "Electric Field Distortions Produced by Solid Dielectric Spacers Separating Uniform Field Electrodes in Nitrobenzene," *1972 Annual Report, Conference on Electrical Insulation and Dielectric Phenomena*, Buck Hill Falls, PA, October, (1972).
- [98] D.C. Wunsch and A. Erteza, "Kerr cell measuring system for high voltage pulses," *Rev. Sci. Instrum.*, 35, pp. 816-820, (1964).
- [99] R.E. Hebner, Jr., R.A. Malewski, and E.C. Cassidy, "Optical methods of electrical measurement at high voltage levels," *Proceedings of the IEEE*, 65, no. 11, pp. 1524-1548, November, (1977).
- [100] R.J. Van Brunt, editor, "Research for Electric Energy Systems - An Annual Report," *NIST Interagency Report*, NISTIR 4339, pp. 60-70, December, (1989).
- [101] J.J. More, "The Levenberg-Marquardt Algorithm: Implementation and Theory," in *Lecture Notes in Mathematics V630 Numerical Analysis* (G. Watson, Ed.), pp. 105-116 Springer-Verlag, Berlin, (1978).
- [102] R.E. Hebner, Jr., R. Sojka, and E.C. Cassidy, "Kerr coefficients of nitrobenzene and water," *NBS Interagency Report* NBSIR 74-544, Washington, D.C., August, (1974).

- [103] R.E. Hebner, Jr. and M. Misakian, "Calibration of high-voltage pulse measurement systems based on the Kerr effect," *NBS Interagency Report NBSIR 77-1317*, Gaithersburg, MD, September, (1977).

NIST-114A
(REV. 3-90)

U.S. DEPARTMENT OF COMMERCE
NATIONAL INSTITUTE OF STANDARDS AND TECHNOLOGY

BIBLIOGRAPHIC DATA SHEET

1. PUBLICATION OR REPORT NUMBER

NISTIR 4931

2. PERFORMING ORGANIZATION REPORT NUMBER

3. PUBLICATION DATE
SEPTEMBER 1992

4. TITLE AND SUBTITLE

Research for Electric Energy Systems - An Annual Report

5. AUTHOR(S)

William E. Anderson, Editor

6. PERFORMING ORGANIZATION (IF JOINT OR OTHER THAN NIST, SEE INSTRUCTIONS)

U.S. DEPARTMENT OF COMMERCE
NATIONAL INSTITUTE OF STANDARDS AND TECHNOLOGY
GAITHERSBURG, MD 20899

7. CONTRACT/GRANT NUMBER

8. TYPE OF REPORT AND PERIOD COVERED

9. SPONSORING ORGANIZATION NAME AND COMPLETE ADDRESS (STREET, CITY, STATE, ZIP)

Department of Energy
Division of Electric Energy Systems
1000 Independence Avenue, SW
Washington, DC 20585

10. SUPPLEMENTARY NOTES

11. ABSTRACT (A 200-WORD OR LESS FACTUAL SUMMARY OF MOST SIGNIFICANT INFORMATION. IF DOCUMENT INCLUDES A SIGNIFICANT BIBLIOGRAPHY OR LITERATURE SURVEY, MENTION IT HERE.)

This report documents the technical progress in the four investigations which make up the project "Support of Research Projects for Electrical Energy Systems", Department of Energy Task Order Number 137, funded by the US Department of Energy and performed by the Electricity Division of the National Institute of Standards and Technology (NIST). The first investigation is concerned with the measurement of magnetic fields in support of epidemiological and in vitro studies of biological field effects. The second investigation is concerned with two different activities: the production of S_2F_{10} in negative corona in SF_6 and the measurement of electron scattering and dissociative electron attachment cross sections for SF_6 and its electrical by-products. The third investigation is also concerned with two different activities: several liquids that are currently used or have potential for use as high voltage dielectrics are studied using conventional impulse breakdown measurement techniques and high-speed photography and advances in partial discharge measurement techniques are presented. The last investigation is concerned with the evaluation and improvement of methods for measuring fast transients in electrical power systems such as might be associated with an electromagnetic impulse.

12. KEY WORDS (6 TO 12 ENTRIES; ALPHABETICAL ORDER; CAPITALIZE ONLY PROPER NAMES; AND SEPARATE KEY WORDS BY SEMICOLONS)

corona discharges; dielectric liquids; electrical insulation; electro-optical measurements; fast transients; gaseous dielectrics; magnetic-field measurements; magnetic field probes; partial discharges; pre-breakdown phenomena; S_2F_{10} ; sulfur hexafluoride

13. AVAILABILITY

UNLIMITED

FOR OFFICIAL DISTRIBUTION. DO NOT RELEASE TO NATIONAL TECHNICAL INFORMATION SERVICE (NTIS).

ORDER FROM SUPERINTENDENT OF DOCUMENTS, U.S. GOVERNMENT PRINTING OFFICE,
WASHINGTON, DC 20402.

ORDER FROM NATIONAL TECHNICAL INFORMATION SERVICE (NTIS), SPRINGFIELD, VA 22161.

14. NUMBER OF PRINTED PAGES

87

15. PRICE

A05

ELECTRONIC FORM

